Representing improved tropospheric ozone distribution over the Northern Hemisphere by including lightning NOx emissions in CHIMERE

Sanhita Ghosh[1], Arineh Cholakian[1], Sylvain Mailler[1, 2], and Laurent Menut[1]

[1]Laboratoire de Météorologie Dynamique, IPSL, École Polytechnique, Route de Saclay, Palaiseau, France, 91128
[2]École des Ponts, Marne-la-Vallée, Institut Polytechnique de Paris

Correspondence: Sanhita Ghosh (ghosh.sanhita@lmd.ipsl.fr; sanhitaghosh027@gmail.com)

Abstract. Estimating nitrogen oxide emissions from lightning (LNOx) in models is highly uncertain, affecting the accuracy of atmospheric composition and air quality assessments. Still, it is essential to include these emissions in models to increase the realism in representing the gases and aerosols. LNOx emissions have recently been incorporated into the updated version of the CHIMERE model (v2023r2). In this study, we evaluate the present state of modelling the lightning flashes over the Northern Hemisphere (NH), using a classical scheme based on cloud top height (CTH) and an updated ice flux-based scheme (ICEFLUX). We conduct a comprehensive 3D comparison of model outputs, including in situ measurements and satellite data, to rigorously assess the robustness and applicability of these parameterizations. The comparative analysis reveals that the CTH scheme provides a more accurate spatial variability of lightning flashes over lands and tropical oceans. Both parameterizations accurately capture the magnitude of lightning flashes over the tropics, while the ICEFLUX scheme is more effective in representing mid-latitudinal flashes. However, both schemes perform well in capturing the seasonal variation of lightning flashes. The estimated flash frequencies over the NH from the experiments closely align with satellite observations, and the LNOx emissions fall within the range reported in previous modeling studies. There is an overall increase in ozone (O_3) concentration due to inclusion of LNOx, which substantially improves the tropospheric O_3 distribution, specifically at the tropical free troposphere. The LNOx emissions hence critically influence the O_3 burden as well as the hydroxyl radicals, which further impact the atmospheric lifetime of trace gas methane.

1 Introduction

Nitrogen oxides (NOx), consisting of nitric oxide (NO) and nitrogen dioxide (NO_2), are trace gases that play a key role in atmospheric chemistry, particularly in the formation of tropospheric ozone (O_3) (Finney et al., 2014; Luo et al., 2017; Akimoto and Tanimoto, 2022). NOx emissions arise from both anthropogenic sources, e.g., fossil fuel combustion, biomass burning, and natural processes, such as lightning and soil-NOx emissions (Verma et al., 2021; Butler et al., 2020). Among these sources, lightning-induced NOx (LNOx) contributes approximately 10%–15% to global NOx emissions, with an even greater contribution (up to 70%) in the upper troposphere (Maseko et al., 2021; Luhar et al., 2021; Wu et al., 2023). Importantly,

LNOx has a stronger impact on tropospheric O_3 formation compared to surface-based sources, due to the altitude at which
25 LNOx is injected into the atmosphere and the efficiency of O_3 production in the upper troposphere (Finney et al., 2016a; Luhar et al., 2021). The mean estimated rate of NOx emissions from lightning is highly uncertain, with recent studies indicating variations ranging between 33–660 moles NO per flash (Luhar et al., 2021; Bucsela et al., 2019; Murray, 2016; Schumann and Huntrieser, 2007); although Schumann and Huntrieser (2007) suggest a mean value of 250 moles NO per flash. In spite of this uncertainties, inclusion of these emissions in models is essential to enhance the accuracy and reliability of model projections.

30 The inclusion of LNOx in chemistry-transport models has been a research topic for several decades (Kang et al., 2020), with seminal studies by Price and Rind (1992); Price et al. (1997a); Schumann and Huntrieser (2007); Allen et al. (2010); Finney et al. (2014), pioneering the quantification of lightning flash rates and their associated NOx production. These foundational studies laid the groundwork for understanding the contribution of LNOx to tropospheric chemistry (Allen et al., 2010; Banerjee et al., 2014; Finney et al., 2016a; Kang et al., 2019, 2020). A range of parameterization schemes, including diverse empirical
35 equations, have been developed over decades to quantify lightning flash rates and their spatial distribution (Finney et al., 2014). Despite the significant progress made, challenges remain in accurately quantifying LNOx emissions, due to uncertainties in characterizing both the spatial and temporal variations in lightning frequency and intensity, the apportionment among 'cloud to ground (CG)' and 'in cloud (IC)' flashes, the rates of NOx production from lightning discharges, as well as the vertical distribution and transportation of LNOx after its generation (Labrador et al., 2005; Schumann and Huntrieser, 2007; Menut
40 et al., 2020a; Wu et al., 2023). Recent studies have focused on improving the representation of lightning in models through various parameterization schemes based on cloud top height (CTH, Price and Rind, 1992; Price et al., 1997a; Clark et al., 2017), ice flux (ICEFLUX, Finney et al., 2014), convective precipitation, updraft of mass flux (Allen et al., 2000; Allen and Pickering, 2002) and convective available potential energy (CAPE, Choi et al., 2005; Zhao et al., 2009). These approaches aim to better capture the spatial and temporal variability of lightning activity, leading to more accurate estimates of LNOx
45 emissions.

In this study, we expand on the previous work by implementing the ICEFLUX scheme in chemistry-transport model CHIMERE and comparing it with the CTH scheme. The CHIMERE model has been developed since 1997 and modified on a regular basis for better prediction of trace gases and aerosols (Menut et al., 2020b). The improvement in the natural emissions in the recent version of the model, allows the incorporation of LNOx emissions (Menut et al., 2024). The study by
50 Menut et al. (2020a), conducted over a short period of two months (July–August, 2013), covering Europe and the northern part of Africa, demonstrates changes in tropospheric O_3 and NOx concentrations resulting from the inclusion of LNOx emissions in CHIMERE, using CTH scheme. However, opportunities remain to improve the representation of flash rates in the model. To address this, we have applied the recent ICEFLUX parameterization. The CTH scheme does not incorporate the complex interactions and charge distributions that drive lightning production (Price and Rind, 1992; Finney et al., 2014), nor does it
55 account for detailed microphysical processes, storm dynamics, and the presence of ice particles (Price and Rind, 1992). The improved modelling of cloud ice has facilitated the inclusion of the upward flux of ice crystals (Finney et al., 2014). However, ice flux alone is insufficient to fully capture the complexities of lightning phenomena, as additional factors likely influence the charging process. Therefore, a comparative analysis of the traditional CTH and the updated ICEFLUX schemes is essential to

assess their effectiveness in the regional model CHIMERE. We perform a 3D comparison of model outputs with each other and with a simulation devoid of LNOx. Model outputs are also compared with in situ measurements and satellite data. Furthermore, validating and evaluating these lightning parameterizations across different models (global and mesoscale) are crucial for fully assessing their robustness and applicability, underscoring the significance of this study. Additionally, a thorough evaluation of simulated tropospheric O_3 is also essential to refine model accuracy and deepen our understanding in the role of LNOx in atmospheric composition.

Furthermore, lightning-generated NOx also influences the tropospheric hydroxyl radical (OH) budget, in addition to affecting O_3 concentrations (Murray et al., 2013; Murray, 2016; Mao et al., 2021). The OH radical is primarily formed due to photolysis of O_3 ($O(^1D)$) at a shorter wavelength ($\leq$330 nm) in the presence of water vapour and secondarily through the reaction between hydroperoxyl radical (HO_2) and NO (Lelieveld et al., 2016; Banerjee et al., 2014). As a highly reactive and short-lived oxidant, with a lifetime of just a few seconds, OH is essential to tropospheric chemistry (Lelieveld et al., 2016). However, substantial variability exists among global models, with differences of up to $\pm$30% in estimating the mean OH burden (Murray et al., 2021). OH further controls the lifetime of many important trace gases, such as methane (CH_4), carbon monoxide (CO) and non-methane volatile organic compounds (NMVOCs) (Akimoto and Tanimoto, 2022; Luhar et al., 2021). For example, increase in OH burden reduces the lifetime of CH_4 (Equation R1), a potent greenhouse gas and a major contributor to global warming (Naik et al., 2013; Banerjee et al., 2014; Murray et al., 2021). By improving the parameterization of LNOx in CHIMERE, this study strengthens our understanding of tropospheric chemistry and the dynamics of trace gases.

$$CH_4 + OH \rightarrow CH_3 + H_2O \tag{R1}$$
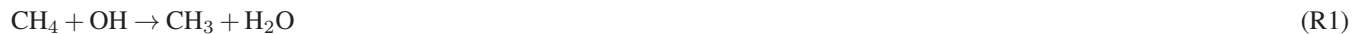
Hence the specific objectives of the study are, (i) to evaluate and improve the modelling of lightning flashes, with the CHIMERE model using the classical CTH and the upgraded ICEFLUX scheme; (ii) to evaluate the effect of LNOx emissions on tropospheric O_3 and trace gases; (iii) the influence on the OH burden and lifetime of CH_4 quantified against the chemical loss. The detailed methodology is provided in Section 2. An analytical evaluation of the simulated results have been carried out and presented in the following sections.

2   Method of study

2.1   CHIMERE model configuration and experimental set-up

In this study, simulations are carried out with the CHIMERE chemistry-transport model (version 2023r2; Menut et al., 2024) over the domain of Northern Hemisphere (NH) expanded from 0°–90°N, at a horizontal resolution of 100×100 km^2. Here, meteorological fields are forced externally to CHIMERE with a 3-hourly forecast dataset from European Centre for Medium-Range Weather Forecasts (ECMWF)– Integrated Forecasting System (IFS) (https://www.ecmwf.int/en/forecasts/datasets, last access: 16 May, 2024). Simulations are done in twenty vertical levels in σ-pressure coordinates ranging from surface to 200

hPa for a period of one year (January–December, 2018) with a spin-up time of 15 days. The MELCHIOR2 scheme is used for the chemical mechanism. The CHIMERE model employs a 10-bin logarithmic sectional size distribution ranging from 0.01 to 40 μm. Fields of chemical concentration are calculated with a time-step of few minutes, using an adaptive time-step, to ensure that the Courant-Friedrichs-Lewy (CFL) stability criterion is satisfied (Menut et al., 2021). Boundary and initial conditions are derived from Copernicus Atmosphere Monitoring Service (CAMS) reanalysis dataset of atmospheric compositions produced by ECMWF, consisting of three-dimensional time-consistent atmospheric composition fields, including aerosols and chemical species (Inness et al., 2019), and from GOCART for dust concentrations (Chin et al., 2002). Biogenic emissions are provided by a reduced online version of the Model of Emissions of Gases and Aerosols from Nature (MEGAN) model (version 2.10) (Guenther et al., 2012). Mineral dust and sea-salt emissions are calculated using the schemes of Alfaro and Gomes (2001) and Monahan (1986), respectively. Anthropogenic emissions in the model are incorporated from CAMS-global and fire emissions are taken from CAMS Global Fire Assimilation System (GFAS, https://atmosphere.copernicus.eu/global-fire-emissions, last access: 16 May, 2024) The formation of SOA is as described in Pun and Seigneur (2007) and Bessagnet et al. (2008). The aerosol dynamic processes, such as condensation, coagulation, wet and dry deposition, absorption, and scavenging, are incorporated into the model (Menut et al., 2021). The mixing state is considered as internal homogeneous aerosol mixing (Menut et al., 2013). The online calculations for radiation and photolysis are incorporated using the FastJX module (Wild et al., 2000; Mailler et al., 2016). The horizontal and vertical transports are solved with the van Leer (1977) scheme. Boundary layer height and vertical diffusion are calculated by the parameterization proposed by Troen and Mahrt (1986) and deep convective fluxes are estimated using the Tiedtke (1989) scheme. Gaseous and aerosol species undergo dry or wet deposition and fluxes are calculated using the Wesely (1989) and Zhang et al. (2001) parameterization schemes. With access to anthropogenic and biogenic emissions, CHIMERE simulates 3D concentration for a range of gaseous and size-resolved particulate species, based on the chosen chemical scheme.

Simulations carried out for this study are (i) not including LNOx emissions (experiment: noLNOx), (ii) including LNOx emissions estimated with parameterization based on cloud top height (CTH) (experiment: LNOx-CTH) and (iii) LNOx emissions estimated with parameterization based on ice flux (experiment: LNOx-ICEFLUX).

2.2 Parameterization of lightning flash

2.2.1 Cloud top height-based parameterization (CTH)

Derived from the theories advanced by Vonnegut (1963) and Williams (1985), Price and Rind (1992) formulated the CTH parameterization, wherein the flash rate is contingent upon the cloud top height (H_{top}). The distinct relationships governing flash rates over land and ocean are delineated as follows:

$$F_l = a \times H_{top}^{4.9}$$
$$F_o = b \times H_{top}^{1.73}$$
(1)

Here, a and b are constants (values are provided in Table 1), H_{top} represents the cloud top height above the ground level in km. Cloud-top height (H_{top}) and bottom height (H_{bottom}) are estimated based on the convection scheme of the model for each time step. F denotes the total flash rate in flash number min^{-1} 25 km^{-2}, with subscripts 'l' and 'o' indicating land and ocean, respectively (Menut et al., 2020a). The distinction between land and ocean is employed to incorporate the disparity in updraft velocity over these two surface types. For instances where the cloud depth ($H_{top} - H_{bottom}$) is less than 5 km, the flash number is set to zero. This threshold reflects the physical condition necessary for charge separation and buildup in a storm to generate lightning. It's noteworthy that Price and Rind (1994) formulated an equation to adapt the above equations to various model resolutions. The scaling factor (C) determined to accommodate the model grid cell size is outlined as follows:

$$C = 0.97241e^{0.048203 \times \Delta x \times \Delta y} \tag{2}$$

Here, the product of longitude and latitude resolution, denoted as $\Delta x \times \Delta y$, is measured in $degrees^2$. This factor typically remains close to 0.97, and its impact on the results is minimal, especially when compared to the uncertainties due to other parameters. These uncertainties are offset by adjustment factors, that align the model more closely to observations (Gordillo-Vázquez et al., 2019). In preliminary simulations, we observed a highly overestimated flash rate, estimated based on the formulations by Price and Rind (1992), compared to the measurements from Lightning Imaging Sensor on the International Space Station (ISS-LIS) for the year 2018, over the land grids, followed by the ocean grids. Considering the overestimation in the modelled flash rate, we have applied factors 0.1 and 0.5, respectively to constants 'a' and 'b' in Equation 1 over the land and ocean grids, in experiment LNOx-CTH, to reconcile the modelled lightning flash rate to the satellite observations (Table 1).

Table 1. Values of constants in Equation 1

constants	Price and Rind (1992)	present study (experiment: LNOx-CTH)
a	3.44×10^{-5}	3.44×10^{-6}
b	6.40×10^{-4}	3.20×10^{-4}

For each grid-cell, the relative fraction of sea (x_{sea}) is determined using the land-sea mask from the land use database (Menut et al., 2020a). The total flash rate (F_{CTH}) is then calculated as follows:

$$F_{CTH} = \frac{C \times (x_{sea} \times F_o + (1 - x_{sea}) \times F_l)}{25} \tag{3}$$

2.2.2 Ice-flux-based parameterization (ICEFLUX)

The equations used to estimate the flash rates in ICEFLUX parameterization are as follows (Finney et al., 2014):

$$f_l = 6.58 \times 10^{-7} \phi_{ice}$$
$$f_o = 9.08 \times 10^{-8} \phi_{ice}$$

$$(4)$$

here, f_l and f_o represent the flash rate (flash number m_{cell}^{-2} s^{-1}) over the lands and ocean, respectively. ϕ_{ice} denotes the upward ice flux (kg_{ice} m_{cloud}^{-2} s^{-1}) at 440 hPa and is determined using the following equation:

$$\phi_{ice} = \frac{q \times \Phi_{mass}}{c}$$

$$(5)$$

In this context, q represents the specific cloud ice water content at 440 hPa (kg_{ice} kg_{air}^{-1}), Φ_{mass} denotes the updraft mass flux at 440 hPa (kg_{air} m_{cell}^{-2} s^{-1}), and c represents the fractional cloud cover at 440 hPa (m_{cell}^{2} m_{cloud}^{-2}). Instances where c is less than 0.01 m_{cloud}^{2} m_{cell}^{-2}, upward ice flux is set to zero. Additionally, if no convective cloud top is identified, the flash rate is also set to zero (Finney et al., 2016a). The total flash rate ($F_{ICEFLUX}$) is then calculated as follows:

$$F_{ICEFLUX} = x_{sea} \times f_o + (1 - x_{sea}) \times f_l$$

$$(6)$$

2.2.3 Distribution of CG and IC lightning flashes

The empirically derived formula used to determine the relative proportion of 'cloud to ground (CG)' flashes in a single thunderstorm is initially based on the cold cloud depth (H_f, from 0°C to cloud top) (Price and Rind, 1993). In this study H_f (in km) is calculated with the temperature profile in the model, estimating the freezing temperature height or the freezing level. The modelled H_f therefore varies from 6.9 to 7.76 km. The freezing level (0°C temperature), estimated in model, varies from 1 to 4.9 km, being the highest at tropics and decreasing with higher latitudes. The flashes from freezing level to the cloud top height is considered as 'in cloud (IC)' flashes and that from freezing level to ground as CG flashes.

The mean ratio of IC to CG flash rates (β = IC/CG) is estimated as 3.09 from model estimates. β, in this study, is estimated with the empirical equation (Equation 7) by Price and Rind (1993), which is frequently used in several modelling studies (Luhar et al., 2021; Gordillo-Vázquez et al., 2019). The empirical relationship between β and the cold cloud depth (H_f) was developed by Price and Rind (1993) based on data collected for 139 individual thunderstorms over the western United States (US) during summer. Several studies support the fact that the parameterization Price and Rind (1993) successfully estimate the distribution of CG and IC flashes in global as well as in mesoscale models (Pickering et al., 1998; Fehr et al., 2004). Theoretically, β varies between 1 to 50 for H_f varying between 5.5 to 14 km to prevent unrealistic values. The value of β estimated in our study is comparable to that obtained in recent modelling studies (Luhar et al., 2021; Gordillo-Vázquez et al., 2019). Wu et al. (2023) estimates the values of β as 2.94–3.70 with a lightning nitrogen oxides (LNOx) emissions model using

satellite-observed lightning optical energy. Further, experiments conducted with satellite- and ground-based observations over different parts of the world also produce a β value in the range of 2.64–2.94 ($\pm$1.1–1.3) over US (Boccippio et al., 2001), 3–4 over India and China (Ghosh et al., 2023; Ren et al., 2024). β obtained in our study again shows consistency with the above mentioned results.

$$\beta = 0.021 H_f^4 - 0.648 H_f^3 + 7.49 H_f^2 - 36.54 H_f + 63.09 \tag{7}$$

The relative part of CG in the total (IC + CG) is denoted by p (Equation 8). The estimated value of p from our study is 0.25, aligning with findings from recent research (Luhar et al., 2021).

$$p = \frac{1}{1+\beta} \tag{8}$$

Hence, the β in our study is not predetermined but is calculated based on the cold cloud thickness (H_f), estimated with temperature profile in CHIMERE and agrees well with the values estimated theoretically and from other model-based studies.

2.3 Estimation of LNOx emissions

Lightning flash energy estimates span a broad range from 0.35 to 5 GJ based on length-specific discharge values to up to 6.7 GJ considering contributions to the global atmospheric electric circuit (Krider et al., 1968; Uman, 2001; Price et al., 1997a). The NOx production rate per unit discharge energy also exhibits substantial variation, ranging from 1.1×10^{16} to 50×10^{16} molecules J^{-1} in laboratory experiments (Schumann and Huntrieser, 2007), and 5–15×10^{16} molecules J^{-1} in theoretical models (Price et al., 1997a). In this study, we adopt flash energies of 3 GJ for CG flashes and 0.9 GJ for IC flashes, along with a NO production rate of 14.2×10^{16} molecules NO J^{-1} (Schumann and Huntrieser, 2007). Using these values, we calculate the NO production in moles per flash as described in Equation 9, yielding a mean value of 332 moles of NO per flash. This estimation considers CG flashes as 25% of the total lightning flashes.

$$
\begin{aligned}
P(\text{CG, NO}) &= 697.44\,\text{moles flash}^{-1}, \\
P(\text{IC, NO}) &= 199.27\,\text{moles flash}^{-1}
\end{aligned}
\tag{9}
$$

Recent research indicates comparable NO production rates for CG and IC lightning flashes, with a mean of 70–700 moles NO per flash (Bucsela et al., 2019; Ott et al., 2010; Finney et al., 2016a; Luhar et al., 2021). Despite this, significant differences in NOx production between IC and CG flashes are well-documented through theoretical models and observational studies, emphasizing the challenges and variability in quantifying NOx production rates (Gordillo-Vázquez et al., 2019; Carey et al., 2016; Koshak et al., 2014; Pickering et al., 1998; Price et al., 1997a). Global modelling efforts, such as those using

National Aeronautics and Space Administration (NASA) Goddard Earth Observing System (GEOS)-5 and GEOS-Chem systems, combined with satellite and airborne observations, have reported lightning NO production rates of 260 moles per flash (Jourdain et al., 2010), 246 moles per flash (Liaskos et al., 2015), and a range of 346 (over tropics) to 665 (for mid-latitude region) moles per flash (Nault et al., 2017). Additionally, Miyazaki et al. (2014) derived a global average of 310 moles NO per flash by integrating lightning data from the Optical Transient Detector (OTD) and the Lightning Imaging Sensor (LIS) with atmospheric composition measurements in a global chemistry-transport model. Overall, the mean NO production varies across 2 to 3 orders of magnitude in moles NO per flash, as noted by Bucsela et al. (2019); Murray (2016); Schumann and Huntrieser (2007), although a mean value of 250 moles NO per flash has been suggested by Schumann and Huntrieser (2007). The estimates derived in this study is close to the values estimated by Miyazaki et al. (2014); Luhar et al. (2021), consistent with prior findings, underscoring the complexity of accurately assessing lightning-induced NO production. The NO_2 emissions are assumed to be 10% of the NO emissions.

2.4 Estimation of CH_4 lifetime due to chemical loss

The loss in tropospheric methane (CH_4) is primarily (90%) due to oxidation by hydroxyl radicals (OH, Reaction R1)(Ghosh et al., 2015). The estimation of tropospheric chemical loss rate of CH_4 is as follows (in molecules cm^{-3} s^{-1}) (Zhao et al., 2023):

$$\text{rate} = k(T)[CH_4][OH] \tag{10}$$

where, $[CH_4]$ and $[OH]$ are the concentrations of CH_4 and OH (in molecules cm^{-3}). $[OH]$ is taken from simulation in CHIMERE from our study, whereas $[CH_4]$ is from chemical boundary conditions. The reaction rate (k(T) in cm^3 molecule^{-1} s^{-1}) is temperature (T) dependent (Burkholder et al., 2019) and is represented in (Menut et al., 2013),

$$k(T) = 2.3 \times 10^{-12} \exp\left(-\frac{1765}{T}\right) \tag{11}$$

The total tropospheric chemical loss of CH_4 (L in Tg yr^{-1}) is estimated as,

$$L_{CH_4} = \int\limits_V k(T)[CH_4][OH]\,dV \tag{12}$$

dV is the differential volume element in the troposphere. The lifetime of CH_4 (τ_{CH_4} in year) is expressed as,

$$\tau_{\text{CH}_4} = \frac{B_{\text{CH}_4}}{L_{\text{CH}_4}} \tag{13}$$

Here, B_{CH_4} is the annual tropospheric burden (in Tg) of CH_4. Note that, all the calculations in our study are done for NH.

2.5 Observation data for evaluation

Flash rate for the year 2018 from Lightning Imaging Sensor (LIS) on the International Space Station (ISS) platform, is used for evaluating flash rate estimated with the model (http://ghrc.nsstc.nasa.gov/; last access: 5 July, 2024). ISS-LIS optically detects lightning flashes that occur within its field-of-view during both day and night with storm-scale (4 km $\times$ 4 km) horizontal resolution (Blakeslee et al., 2020) and 2 ms of temporal resolution. After time corrections comparing with Geostationary Operational Environmental Satellite (GOES) 16 and 17 Geostationary Lightning Mappers (GLM-16/17) and ground-based observations, the timing accuracy of ISS-LIS is better than its native precision of 2 ms. The flash detection efficiency of ISS-LIS is around 60% with diurnal variability of 51%–75% (Blakeslee et al., 2020). Monthly averaged flash rates are obtained from combined climatology product of satellite observations from the Optical Transient Detector (OTD) and the Lightning Imaging Sensor (LIS), launched with the MicroLab-1 satellite, for the period of May, 1995 to December, 2014 (http://ghrc.nsstc.nasa.gov/; last access: 21 November, 2024). The product utilized in this study is the High Resolution Monthly Climatology (HRMC), which offers 12 monthly values at a horizontal resolution of $0.5° \times 0.5°$. Details are provided in Cecil et al. (2014).

For evaluating the vertical profile of O_3, altitudinal data measured by ozone-sonde, launched on small balloons, are downloaded from the World Ozone and Ultraviolet Radiation Data Centre (WOUDC, https://woudc.org/data, last access: 5 July, 2024) for the year 2018. Ozone-sonde data from 122, 977 and 121 stations are collected, respectively, over the tropical (0°–30°N), mid-latitudes (30° N–60° N) and polar region (60° N–90° N). We also have used vertical O_3 profile data from Southern Hemisphere ADditional OZonesondes (SHADOZ) ozone-sonde measurements (https://tropo.gsfc.nasa.gov/shadoz, last access: 21 November, 2024) at four tropical stations (Kuala Lampur: 3.14°N, 101.69°E; Hanoi: 21.02°N, 105.80°E; Costa Rica: 9.62°N, $-84.25°$E and Hilo: 19.72°N, $-155.08°$E) for the year 2018. Global distributions of tropospheric column of ozone (TCO) are derived from the Ozone Monitoring Instrument (OMI) and Microwave Limb Sounder (MLS) on board the Aura satellite (https://acd-ext.gsfc.nasa.gov/; last access: 5 July, 2024) for the year 2018. The monthly mean TCO data from OMI/MLS are derived by subtracting the stratospheric column of ozone (SCO) from the total column of ozone measured by the OMI sensor. This process utilizes the tropospheric ozone residual (TOR) algorithm along with stratospheric ozone profile information from the MLS sensor (Ziemke et al., 2006). The dataset covers the spatial range of $\pm60°$ with a spatial resolution of $1° \times 1.25°$, spanning the period from October 2004 to December 2020.

This study utilizes total tropospheric column NO_2 from daily global gridded ($0.25° \times 0.25°$) NO_2 Product from OMI L3-level (https://data.gesdisc.earthdata.nasa.gov/; last access: 2 December, 2024) for the year 2018 (Levelt et al., 2018). OMI is an ultraviolet-visible (UV-Vis) spectrometer on the polar-orbiting NASA Aura satellite, launched on 15 July, 2004 (Lamsal et al., 2021). The simulated O_3 and NO_2 mixing ratio is compared with ground-based observation data from Ope-

nAQ (https://openaq.org; last access: 5 July, 2024; Hasenkopf et al., 2015), U.S. Environmental Protection Agency (EPA, https://www.epa.gov; last access: 5 July, 2024), European Environment Agency (EEA, https://www.eea.europa.eu; last access: 5 July, 2024), Environment and Climate Change Canada (ECCC) data catalogue (https://data-donnees.az.ec.gc.ca, last access: 5 July, 2024), Subsistema de Informacion de Calidad del Aire (SISAIRE, http://sisaire.ideam.gov.co; last access: 5 July, 2024)

250 and China National Environmental Monitoring Centre (CNEMC, https://quotsoft.net/air/; last access: 5 July, 2024; Dufour et al., 2021), collected over the study period. The total number of observation stations over the NH are mentioned in Table 6. The evaluation of simulated data is done with the statistical analyses estimating the mean absolute bias (MAB), normalized mean error (NME), and root mean square error (RMSE), using the annual mean of O_3 and NO_2 mixing ratio.

3 Results and Discussions

255 ### 3.1 Evaluation of modelled lightning flash rate

In this section we analyse the estimated lightning flash rates over the Northern Hemisphere (NH), from simulations conducted with CHIMERE model applying parameterization schemes based on cloud top height (experiment: LNOx-CTH) and ice flux (experiment: LNOx-ICEFLUX). The modelled flash rates from the two simulations are compared with observed flash rates from ISS-LIS (domain: $\pm 55°$ latitudes) for the year 2018 and the combined climatology product of satellite observations from

260 the OTD/LIS for the period of May, 1995 to December, 2014. The spatial distribution of annual flash rates are presented in Figure 1. Please note that the flash rates over the land, estimated with ICEFLUX parameterization, are divided by 5 for each grid to match the ISS-LIS satellite observations.

As observed from our study, warm tropical regions (0°–30°N), especially central Africa, south America, India and south China are the regions with high lightning flash rate due to large convective activity, followed by the mid-latitudes (30° N–

265 60°N; Figures 1c and 1d). South Asia, including India and south China, where significant flash rates are observed, are known to exhibit the greatest seasonal and interannual variation in lightning activities (Pawar et al., 2012a; Xu et al., 2023). The annual flash rate is observed as 10–20 flashes km^{-2} yr^{-1} from both the experiments, over most of the tropical lands (Figures 1c and 1d), which is in agreement to the satellite observations from ISS-LIS and LIS/OTD (Figures 1a and 1b). Over the mid-latitudes, flash rates are observed in the range 2–4 flashes km^{-2} yr^{-1}, while the polar regions (60° N–90°N) exhibit significantly lower

270 values (0.1–0.2 flashes km^{-2} yr^{-1}) as indicated by the simulations as well as the satellite observations. Therefore, the tropical and mid-latitude land regions dominate lightning activity. The spatial distribution of flash rates closely resembles the patterns observed in previous model-based studies using CTH and ICEFLUX schemes (Luhar et al., 2021; Gordillo-Vázquez et al., 2019; Finney et al., 2014, 2016a; Murray, 2016). However, patches of high flash rate observed in satellite data over central Canada, the United States, central European countries, and northern Russia are not reflected in the modelled flash rates from

275 either experiment. Additionally, the elevated flash rates over central Asia are not captured in the LNOx-CTH simulation. Flash rates over land are significantly higher than the oceans due to intense convection over land regions (Albrecht et al., 2016). In oceanic regions, relatively higher flash rates (1–2 flashes km^{-2} yr^{-1}) are observed in the tropical regions, particularly over the Bay of Bengal and the Pacific Ocean, as simulated in LNOx-CTH experiment. Previous studies have reported inconsistencies
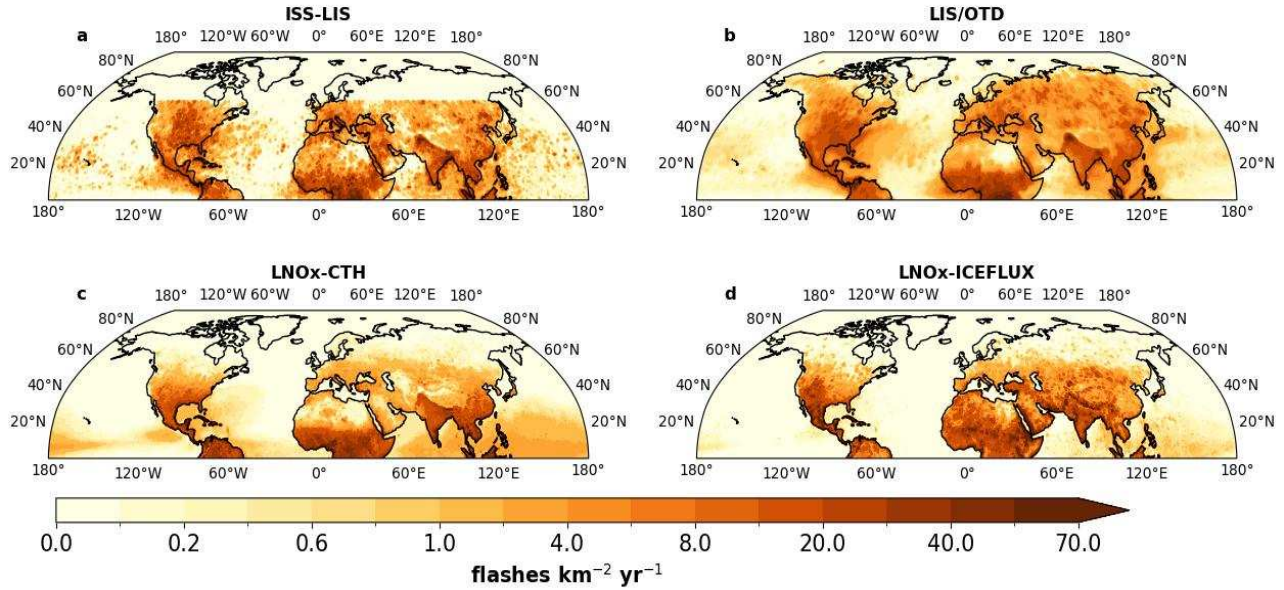
Figure 1. Spatial distribution of annual flash rates (flashes km^{-2} yr^{-1}) over NH based on (a–b) observations from (a) ISS-LIS satellite for the year 2018 (domain: 0–55°N) and (b) OTD/LIS climatology data (May, 1995 to December, 2014), (c–d) simulation experiments (c) LNOx-CTH and (d) LNOx-ICEFLUX.

in the equation for oceanic flashes developed by Price and Rind (1992) (Michalon et al., 1999; Boccippio, 2002; Luhar et al., 280 2021). However, our study demonstrates an improved flash rate distribution over tropical oceans, using the CTH scheme, compared to previous research (Luhar et al., 2021; Finney et al., 2016b). The magnitude of oceanic flash rates are significantly lower in simulations using the ICEFLUX scheme compared to the CTH scheme. ICEFLUX parameterization is based on charging theory, which is not enough to differentiate land and ocean flashes, e.g., more energetic less frequent flashes over oceans (Finney et al., 2014).

Table 2. Mean annual flash rate over NH, lands and ocean in NH for three latitude bands

Name of the experiments	mean flash rates (flashes km^{-2} yr^{-1}) 0°–30°N	30°–60°N	60°–90°N
NH			
LNOx-CTH	4.69	0.86	0.18
LNOx-ICEFLUX	4.55	1.54	0.36
Land in NH			
LNOx-CTH	10.95	1.46	0.55
LNOx-ICEFLUX	12.45	3.92	1.1
Ocean in NH			
LNOx-CTH	0.75	0.2	0.0003
LNOx-ICEFLUX	0.37	0.1	0.0002

Table 3. Statistical analysis of spatially varying annual flash rates from model comparing with ISS-LIS (OTD/LIS) satellite observations over NH, land and ocean in NH for three latitude bands. Latitudinal coverage for the ISS-LIS data is $0°–55°N$. Statistical scores for comparison of simulated flash rates with OTD/LIS observations are provided in the parenthesis.

Name of the experiments	$r^{\perp}$			RMSE (flashes km^{-2} yr^{-1})$^{\perp}$			NME (%)$^{\perp}$		
	$0°–30°N$	$30°–60°N$	$60°–90°N$	$0°–30°N$	$30°–60°N$	$60°–90°N$	$0°–30°N$	$30°–60°N$	$60°–90°N$
	NH								
LNOx-CTH	0.59 (0.73)	0.53 (0.66)	(0.5)	8.21 (6.64)	4.20 (4.06)	(1.15)	93.54 (65.28)	80.37 (76.15)	(96.77)
LNOx-ICEFLUX	0.31 (0.41)	0.28 (0.36)	(0.26)	12.23 (11.35)	5.70 (5.50)	(1.15)	119 (97.65)	108.11 (90.67)	(96.92)
	Land in NH								
LNOx-CTH	0.68 (0.82)	0.64 (0.63)	(0.3)	11.65 (9.52)	4.28 (5.15)	(3.22)	61.41 (37.68)	75.48 (74.34)	(96.88)
LNOx-ICEFLUX	0.15 (0.21)	0.27 (0.34)	(0.12)	21.50 (21.33)	9.34 (8.77)	(3.23)	110.65 (92.57)	154.87 (93.60)	(97.10)
	Ocean in NH								
LNOx-CTH	0.06 (−0.28)	0.15 (0.63)	(−0.1)	0.94 (0.61)	0.41 (0.35)	(0.10)	132.10 (87.88)	101.65 (94.26)	(100)
LNOx-ICEFLUX	0.06 (0.17)	0.14 (0.15)	(−0.1)	0.94 (0.69)	0.42 (0.37)	(0.10)	99.88 (98.88)	100 (99.88)	(100)

$^{\perp}$Correlation coefficient (r), RMSE and NME are estimated comparing simulated flash rates and ISS-LIS (OTD/LIS) satellite observations for the spatially varying annual mean flash rates.
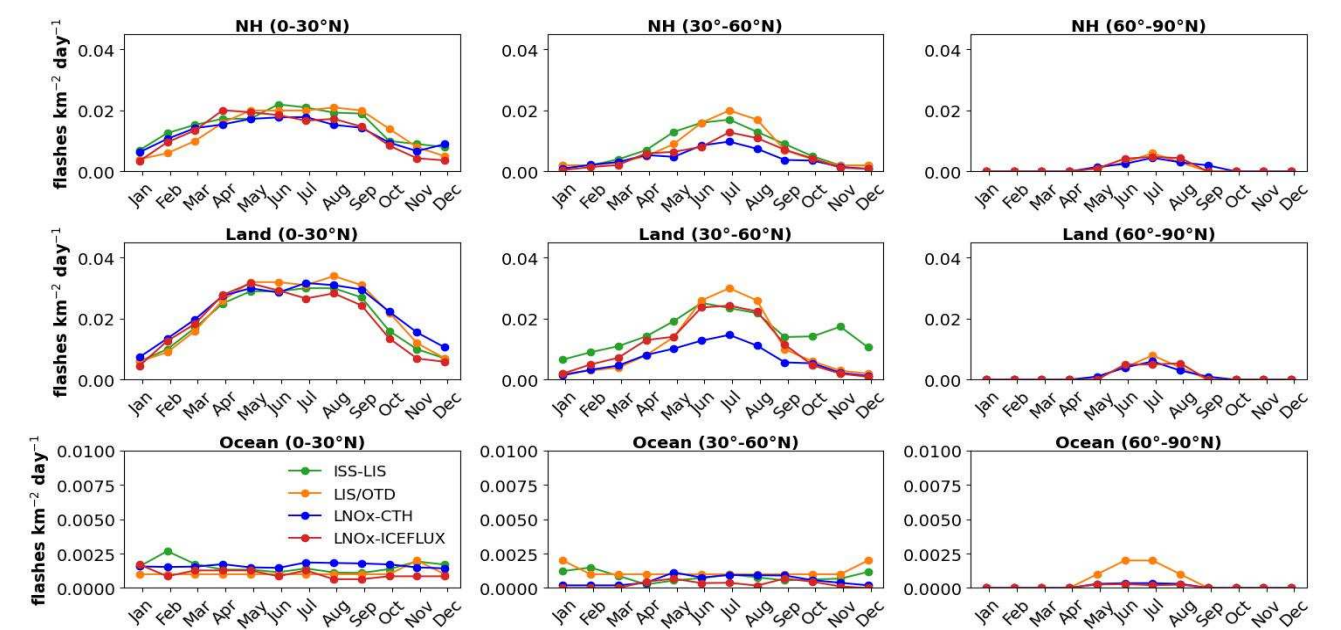
Figure 2. Comparison of monthly mean flash rates (flashes km^{-2} day^{-1}) from simulations (LNOx-CTH and LNOx-ICEFLUX) with ISS-LIS satellite observations for the year 2018 (domain: $0–55°N$) and OTD/LIS monthly climatology (May, 1995 to December, 2014), over NH, land and ocean in NH for the three latitude bands. Please note that the Y-axis in the plots for oceans is presented on a different scale.

285   The spatial mean of annual flash rate over the NH tropics and NH tropical lands are comparable from two experiments, whereas, the flash rate from LNOx-CTH is lower than that from LNOx-ICEFLUX, by a factor of two at mid-latitudes (Table 2). These flash rates over tropics are 5–8 times higher than the mid-latitudes for NH and lands, as estimated from experiment

with CTH. These factors are comparatively lower from experiment with ICEFLUX and from satellite observations, explaining the effectiveness of ICEFLUX scheme over CTH, in capturing flashes over the mid-latitudes. In CTH scheme, the estimated flash numbers are dependent on the cloud top height, which is limited by the tropopause height. The tropopause height is highest at equator and decreases away from the equator (refer to Table S1 in supplementary material presenting the tropopause and cloud top height). This restricts the cloud development to lower altitudes, resulting in a significant reduction in flash rates at higher latitudes (Finney et al., 2014). Spatially mean annual flash rates over tropical lands from both the experiments are close enough to the satellite measurements at tropics over NH and lands, while at mid-latitudes, only a good resemblance is observed for that from LNOx-ICEFLUX. On the other hand, the simulation with CTH scheme estimates the flash rates over tropical ocean as almost twice of that estimated using the ICEFLUX scheme, unlike that showed in previous studies (Finney et al., 2016b). We compare the spatially varying simulated annual flash rates with satellite observations (ISS-LIS and OTD/LIS) and the corresponding statistical metrics are presented in Table 3. Correlation coefficients for spatially varying flash rates show comparatively stronger correlations over the tropics and mid-latitudes of the NH and land regions, between that from LNOx-CTH and satellite data, compared to LNOx-ICEFLUX, being consistent with the findings by Clark et al. (2017). The flash rates from LNOx-CTH exhibit significantly higher correlations, particularly when evaluated against OTD/LIS data. Analysis of RMSE and NME also indicates lower errors for LNOx-CTH over these regions in comparison to that observed for LNOx-ICEFLUX, indicating the spatial variations of flashes from the first experiment align well with the satellite data. The worst performance is observed in the polar lands compared to the other two latitude bands, and also over oceanic region from both the experiments, characterized by weak correlations and higher errors. Hence, both schemes struggle to accurately simulate flash rates over oceans and high latitude lands. However, since lightning activity is minimal in these regions, the impact of this limitation is relatively minor. These results also highlight the ongoing challenges of accurately representing convection and capturing lightning flashes over the oceans. In summary, the statistical analysis points out the effectiveness of the LNOx-CTH scheme in reproducing the spatially varying lightning flash rates reasonably well, particularly at tropics over NH and lands. However, both parameterizations exhibit limitations in the polar regions and over oceans, indicating scopes for further improvement in the parameterizations. Despite its lower overall performance in capturing spatial variation of flashes, LNOx-ICEFLUX shows lower bias in magnitude over mid-latitudinal land regions, suggesting the potential for refinement.

Figure 2 compares the monthly averaged lightning flash rates across different latitude bands in the NH, over land and ocean regions. The figure incorporates satellite observations (ISS-LIS and LIS/OTD) and results from two simulation experiments (LNOx-CTH and LNOx-ICEFLUX). Flash rates from the LNOx-CTH experiment show a clear seasonal cycle, with peaks occurring in May–August over NH and lands. During the winter months (November–January), flash rates drop significantly, being 5–7 times lower than the summer (May–August) peak values. The seasonal variation observed in the LNOx-ICEFLUX experiment and satellite observations closely align with this trend. Over land, both observations and simulations indicate high flash rates, particularly in the tropics, followed by mid-latitudes for all the months. Peak lightning activity over lands occurs during late spring and early summer (May–August), corresponding to enhanced convective activity (Holle et al., 2016; Ghosh et al., 2023). In contrast, flash rates over oceans are consistently lower over all latitude bands. The tropical ocean shows an uniform flash rates throughout the year, without any prominent seasonality. The delay in the seasonal peak of flash rates over

NH with CTH, and particularly with ICEFLUX, as noted by Finney et al. (2014), is not seen in our simulations. Therefore, using near-real-time, high spatially and temporally resolved meteorological data from ECMWF-IFS with continuous updates

325 and improved configuration for advection in CHIMERE, we achieve an improved seasonal distribution that match well the satellite measurements.

Table 4. Statistical analysis of monthly mean flash rates from model comparing with ISS-LIS (OTD/LIS) satellite observations over NH, land and ocean in NH for three latitude bands. Statistical scores for comparison of simulated flash rates with OTD/LIS observations are provided in the parenthesis.

Name of the experiments	r[‡]			NME (%)[‡]		
	0°–30°N	30°–60°N	60°–90°N	0°–30°N	30°–60°N	60°–90°N
			NH			
LNOx-CTH	0.86 (0.84)	0.83 (0.94)	(0.97)	17.4 (24.5)	44.3 (43.1)	(34.6)
LNOx-ICEFLUX	0.92 (0.85)	0.89 (0.92)	(0.81)	24.8 (22.4)	33.6 (33.5)	(29.2)
			Land in NH			
LNOx-CTH	0.92 (0.98)	0.87 (0.97)	(0.97)	16 (11.3)	56.7 (41.1)	(23.5)
LNOx-ICEFLUX	0.92 (0.93)	0.85 (0.96)	(0.85)	23.4 (16.9)	31.5 (20.6)	(37.6)
			Ocean in NH			
LNOx-CTH	−0.1 (−0.28)	−0.48 (−0.49)	(0.87)	27.5 (57.3)	57.2 (53.7)	(78.3)
LNOx-ICEFLUX	0.04 (−0.17)	−0.74 (−0.49)	(0.88)	34.5 (32.9)	76.2 (76.5)	(83.8)

[‡]correlation coefficient (r) and NME estimated comparing simulated monthly mean flash rates and the same from ISS-LIS (OTD/LIS) satellite observations.

Table 5. Estimated flash frequencies and LNOx emissions from simulations over NH. Flash frequencies in parenthesis are estimated for the domain 0–55°N, comparable to the ISS-LIS satellite data (23.6 flash s^{-1}). The flash frequencies from OTD/LIS climatology data are 26.4 and 25.3 flash s^{-1} over NH and for the domain 0–55°N.

Name of experiments	flash frequency (flash s^{-1})	total LNOx emissions (Tg N yr^{-1})	correction factor
LNOx-CTH	20.7 (20.64)	2.8	none
LNOx-ICEFLUX	21.6 (21.53)	3.1	5

The modeled monthly averaged flash rates from the simulations exhibit a strong positive correlation with satellite observations (ISS-LIS and OTD/LIS), with correlation coefficients ranging from 0.85 to 0.97 (Table 4). This agreement is consistent across all latitude bands over the NH, land regions, and the polar ocean region from both the experiments (LNOx-CTH and

330 LNOx-ICEFLUX). These findings indicate that the simulations successfully capture the seasonal variability of flash rates. In contrast, a weaker negative correlation is observed over tropical and mid-latitudinal oceans, indicating an inverse relationship between simulated and observed seasonality in flash rates in these regions. When comparing the simulated monthly flash rates with satellite observations, the results from LNOx-CTH align more closely with satellite observations at tropics than the mid-latitudes, as evidenced by lower NME at tropics over NH, land and ocean regions. Notably, the simulation LNOx-ICEFLUX

335 exhibits a better performance at mid-latitudes than the LNOx-CTH, over NH and land regions, specially while compared with

OTD/LIS measurements. Further, advancement in the seasonal representation of oceanic convection processes is essential for improving the simulation of flash rates over oceans.

The annual flash frequencies over the NH is estimated as 20.7 and 21.6 flashes s^{-1}, respectively from the LNOx-CTH and LNOx-ICEFLUX experiments (Table 5). These values are consistent with the satellite observations (23.6 and 26.4 flashes s^{-1},
340 respectively from ISS-LIS and OTD/LIS observation over NH) as well as to that obtained in recent model-based studies over NH (Luhar et al., 2021). While no scaling factor is applied in the simulated flash rates from LNOx-CTH, the flash frequency from LNOx-ICEFLUX is divided by a factor 5 to reconcile with the satellite-observed frequency. Accordingly, the evaluation of the results from LNOx-ICEFLUX has been conducted using flash rates adjusted by this factor. For instance, a recent study by Finney et al. (2016a) utilizing the UK Chemistry and Aerosol (UKCA) model determined that the global flash rate scaling
345 factors required for the UKCA model are 1.44 and 1.12 for the CTH and ICEFLUX lightning parameterizations, respectively. Another study by Gordillo-Vázquez et al. (2019) produce scaling factors 2.05 and 4, respectively for the CTH and ICEFLUX lightning schemes in Community Atmosphere Model (CAM5). The factors may vary up to 2–3 orders of magnitude to match observations, based on the lightning parameterization used and the results obtained (Tost et al., 2007; Finney et al., 2014).

In CTH parameterization, the assumption of minimum required cloud depth of 5 km, may introduce uncertainty in estimating
350 lightning flashes, as it inherently assumes that every convective cloud with depth of 5 km corresponds to a thunderstorm (Luhar et al., 2021). It would be worthwhile to investigate the sensitivity of the modeled flash rates to the minimum cloud depth by varying this arbitrary threshold, either increasing or decreasing it. Similarly, the estimated flash numbers are very much sensitive to the choice of pressure levels for calculating ice flux in the ICEFLUX parameterization (Finney et al., 2014). For example, it performs better at lower pressure levels (e.g., 340 and 440 hPa) but shows diminished correlations at higher
355 pressure levels (e.g., 540 hPa). This sensitivity complicates its application across different regions and scales. Uncertainty also arises from the input meteorological data, model configuration and the detection efficiency of satellite measurements is also a significant factor when comparing the modeled flashes with satellite observations (Blakeslee et al., 2020; Erdmann et al., 2020; Zhang et al., 2023).

3.2 NOx emissions from lightning

360 The production of LNOx emissions depends on the average flash frequency (in flashes s^{-1}) and the NOx production efficiency per flash, which represents the rate of NOx emissions per flash (Schumann and Huntrieser, 2007; Gordillo-Vázquez et al., 2019; Bucsela et al., 2019; Luhar et al., 2021). In this study, the mean LNOx emission per flash is estimated as 332 mol. The estimated annual NO emissions from lightning are 2.8 Tg N yr^{-1} and 3.1 Tg N yr^{-1} over the NH, respectively from LNOx-CTH and LNOx-ICEFLUX simulations (Table 5). Notably, LNOx emission from LNOx-ICEFLUX is 7.5% higher than
365 that from LNOx-CTH. Recent studies estimate global LNOx emissions typically range from 2 to 8 Tg N yr^{-1} (Schumann and Huntrieser, 2007; Finney et al., 2016b; Nault et al., 2017), with variations reaching up to 25 Tg N yr^{-1} in extreme scenarios (Price et al., 1997a, b). Price et al. (1997b) suggested that, the global annual LNOx emissions cannot be less than 5 Tg N or exceed 25 Tg N. The LNOx emissions from our study align well with the estimates by Luhar et al. (2021), which ranged from 2.39 to 3.41 Tg N yr^{-1} over the NH when using CTH and a new parameterization by Luhar et al. (2021). A recent study
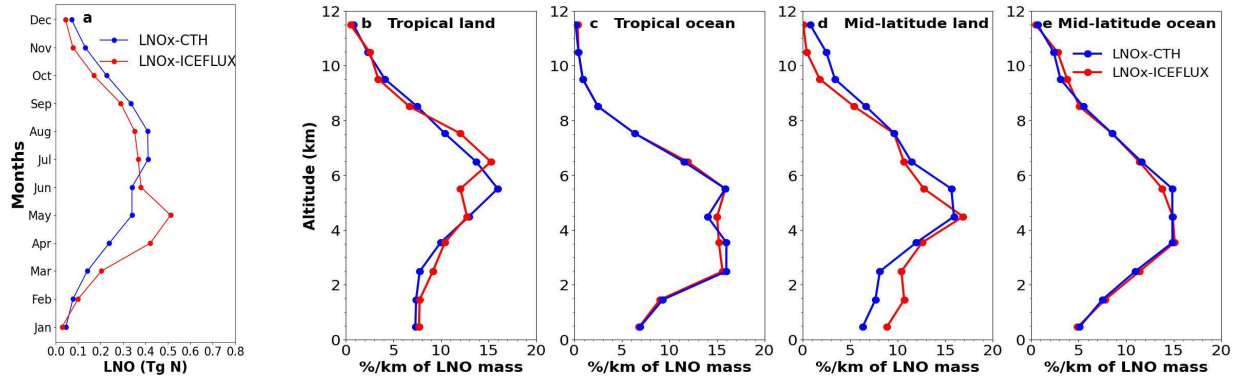
Figure 3. (a) Monthly LNOx emissions in Tg N from simulations LNOx-CTH and LNOx-ICEFLUX. (b–e) Vertical distribution of percentage of annual LNOx mass per kilometer from simulations LNOx-CTH and LNOx-ICEFLUX averaged over (b) tropical land, (c) tropical ocean, (d) mid-latitudinal land and (e) mid-latitudinal ocean.

370 shows that the estimated global LNOx emissions, with CTH scheme and the new parameterization by Luhar et al. (2021), are respectively 5.66 and 5.58 Tg N yr^{-1} in the model EMAC (Pérez-Invernón et al., 2024). These estimates are respectively, 17% higher and 15% lower than that estimated by Luhar et al. (2021) with the same parameterizations, showing the LNOx emissions are highly sensitive to the model configurations. The monthly variation in LNOx emissions, in our study, from the two simulations is shown in Figure 3a. The results indicate that peak emissions occur in July–August, followed by May–June

375 and September, in the LNOx-CTH experiment. The emissions from the LNOx-ICEFLUX experiment peak in May, followed by the remaining summer months (April, June–August). Approximately 60%–70% of the total annual LNOx emissions are contributed during late spring and summer (April–August), when lightning activity is at its highest.

The Figures 3b–3e represent the vertical distribution of LNOx emissions as percentage of LNOx mass per km. The distribution shows the maximum of LNOx mass lies between the altitude range of 4–7 km at all regimes from both the simulations,

380 showing the typical 'backward C-shape' (Ott et al., 2010). 60–65% of LNOx mass is injected at this altitude range. Here it is to be mentioned that annually 1.85 and 1.9 Tg N LNOx are being generated over tropical land as obtained from LNOx-CTH and LNOx-ICEFLUX simulations, respectively, being almost 63%–66% of total annual LNOx over NH. The amounts are 0.55 (0.76), 0.15 (0.09) and 0.07 (0.03) Tg N for mid-latitudinal land, tropical ocean and mid-latitudinal ocean respectively, from LNOx-CTH (LNOx-ICEFLUX) simulation. Therefore, the mid-tropospheric region (4–8 km) contributes the maximum of the

385 LNOx mass, specially over the tropical land region. The vertical profiles available from previous studies reveal a similar shape of all the profiles but contributing maximum at upper tropospheric region (within 2–4 km of the tropopause) rather than mid-troposphere. However, the study by Pickering et al. (1998) represents a high emission near surface due to strong downdraft, where the distribution is low and almost uniform up to 5–6 km as observed from the studies by Ott et al. (2010); Luhar et al. (2021). Nevertheless, the profile over mid-latitude lands from our study matches well with that from the study by Ott et al.

390 (2010), with a maximum at 5 km. In our study, 13%–19% of total LNOx mass is estimated from surface to up to 2 km over tropical and mid-latitude lands and tropical oceans. LNOx production is suggested to be proportional to atmospheric pressure

by Goldenbaum and Dickerson (1993); Pickering et al. (1998). Notably, a simple vertical structure of the emissions is adopted in this study, considering the emissions to be evenly distributed over an altitude range. The vertical distribution of LNOx mass can be improved by replacing the simple distribution currently used, with the more detailed scheme developed by Pickering et al. (1998).

3.3 Vertical distribution of gases: effects of LNOx

3.3.1 Ozone

Numerous studies have demonstrated that LNOx emissions play a significant role in influencing the levels of ozone and other trace gases as a result of the oxidation of CO, CH_4 and volatile organic compounds (VOCs), particularly in the free troposphere (Luhar et al., 2021; Mao et al., 2021; Finney et al., 2016b; Liaskos et al., 2015). The changes in the annual mean of O_3 mixing ratio, due to the inclusion of LNOx in simulation LNOx-CTH, with respect to that from simulation noLNOx, averaged over four altitude bands (998–900, 900–750, 750–500 and 500–200 hPa) is presented in Figure 4. The changes in the same from experiment LNOx-ICEFLUX with respect to LNOx-CTH, are also produced in Figure 5. The highest increase in simulated O_3 is observed in the altitude band 750–500 hPa, specifically over the tropics, by 6–10 ppbv. 4–6 ppbv increase over the tropics is also observed at the altitude bands 900–750 hPa and 500–200 hPa (mid- to upper troposphere). The increase is maximum over the tropical region of America, central Africa, southern Asia and the Maritime continents in south-east Asia (Indonesia, Philippines and Malaysia). The above-mentioned regions with comparatively larger increase in O_3, identified for all the altitude bands, are observed as regions with the largest convection depth and LNOx emissions (Banerjee et al., 2014). A higher value by 2–4 ppbv in annual mean O_3 is also observed from LNOx-ICEFLUX, with respect to LNOx-CTH over the tropical region for the altitude band 750–500 hPa, followed by 900–750 hPa band (Figure 5). Even higher increase over the tropical region of America, central Africa and Tibetan Plateau is also found from LNOx-ICEFLUX. On the other side, the changes in O_3 mixing ratio are insignificant over mid-latitudes and polar regions from both the simulations with respect to noLNOx. The percentage changes in the annual mean of O_3 mixing ratio from LNOx-CTH with respect to noLNOx, averaged over selected latitude and altitude bands present an overall improvement in tropospheric O_3 (Table S2 in supplementary). O_3 levels are significantly elevated by 10%–19% in the mid and upper troposphere (750–200 hPa), where O_3 production occurs efficiently (Dahlmann et al., 2011). Tropical mid- and upper tropospheres are more crucial in O_3 production as most lightning discharges occur in these regions (Luhar et al., 2024; Bucsela et al., 2019; Murray, 2016). A moderate (3%–5%) to low (1%–2%) increase in mid and upper tropospheric O_3 is also observed over mid-latitudes followed by the polar region. Higher O_3 mixing ratios are observed in LNOx-ICEFLUX compared to LNOx-CTH in the mid to upper troposphere across all latitude bands, likely due to comparatively higher LNOx production from LNOx-ICEFLUX in these regions.

Figure 6 represents the vertical profile of annual mean O_3 mixing ratio from simulations and their comparison with the WOUDC ozone-sonde measurements, averaged for the stations over three latitude bands (0°–30° N, 30° N–60° N and 60° N–90° N). The upper tropospheric O_3 mixing ratio is moderately higher than that observed at surface at the tropics by 30%–60%, while it is 2–3 times higher over the mid-latitudes and polar region as observed from simulation LNOx-CTH (Table S2
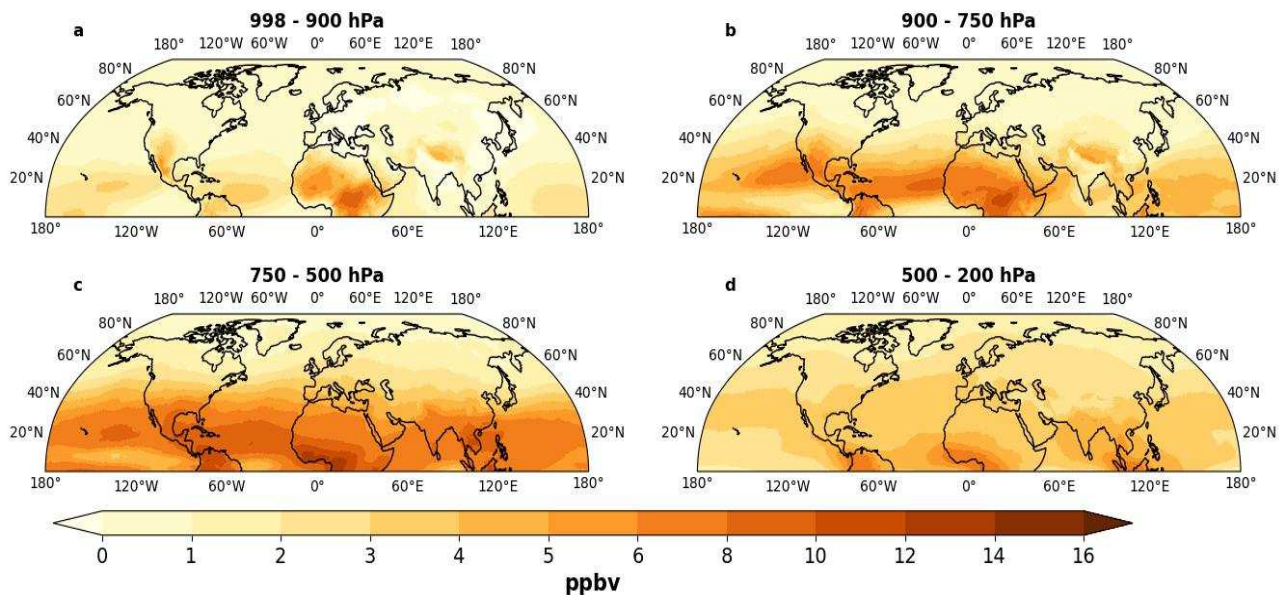
Figure 4. Changes in annual mean of O$_3$ mixing ratio from experiment LNOx-CTH w. r. t. noLNOx (ΔO$_3$) at the altitude bands of (a) 998–900 hPa, (b) 900–750 hPa, (c) 750–500 hPa and (d) 500–200 hPa; positive and negative values represent the increase and decrease in the O$_3$ mixing ratio, respectively.
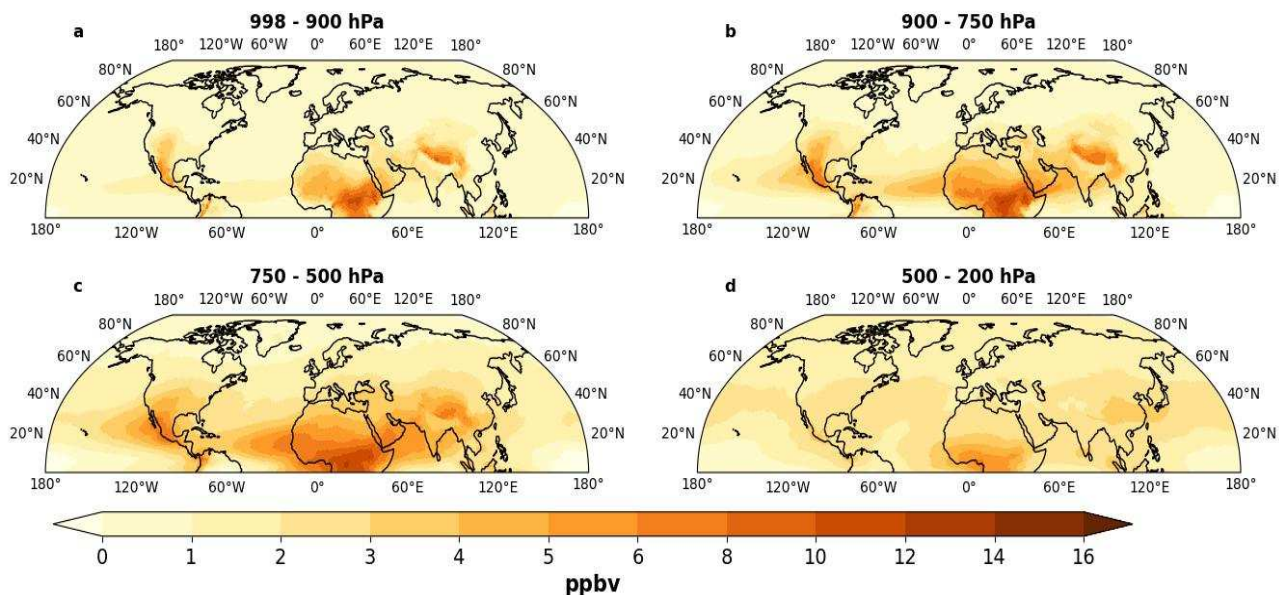
Figure 5. Changes in annual mean of O$_3$ mixing ratio from experiment LNOx-ICEFLUX w. r. t. LNOx-CTH at the altitude bands of (a) 998–900 hPa, (b) 900–750 hPa, (c) 750–500 hPa and (d) 500–200 hPa; positive and negative values represent the increase and decrease in the O$_3$ mixing ratio, respectively.

425 in supplementary). The upper tropospheric O_3 over the polar region is also almost twice of that over the tropics (Table S2 in supplementary). Notably, the vertical profile from observations represents an increasing O_3 mixing ratio with altitude, whereas, those from simulations show an overestimated O_3 mixing ratio near surface which tend to decrease near the boundary layer in the tropics (Figure 6). The simulated O_3 is also observed to be higher near surface and show a continuous increasing pattern over mid-latitudes and polar regions. It is visible in Figure 6, that the simulated O_3 mixing ratio from the experiments with LNOx,

430 represents the measured O_3 adequately well, specifically in the free troposphere over tropics, where a large underestimation is observed in simulated O_3 from noLNOx simulation. The absolute bias in simulated O_3 in the free troposphere, especially over the tropics, is reduced due to inclusion of LNOx in the model (Table S3 in supplementary). The bias is however lower for that from LNOx-CTH in comparison to LNOx-ICEFLUX. O_3 production efficiency due to LNOx is higher in the mid to upper troposphere, primarily because lower temperatures extend the lifetime of NOx, while enhanced photolysis rates further

435 favour O_3 accumulation (Labrador et al., 2005). The high underestimation in the simulated O_3 mixing ratio in the altitude band 500–200 hPa, i.e., the upper troposphere and lower stratosphere, over mid-latitudes and polar regions still exists, even after the inclusion of LNOx, however lower underestimation is observed for LNOx-ICEFLUX. The underestimation represents that improvement in the modelled stratosphere-troposphere exchange still requires a lot of refinement and further investigation.
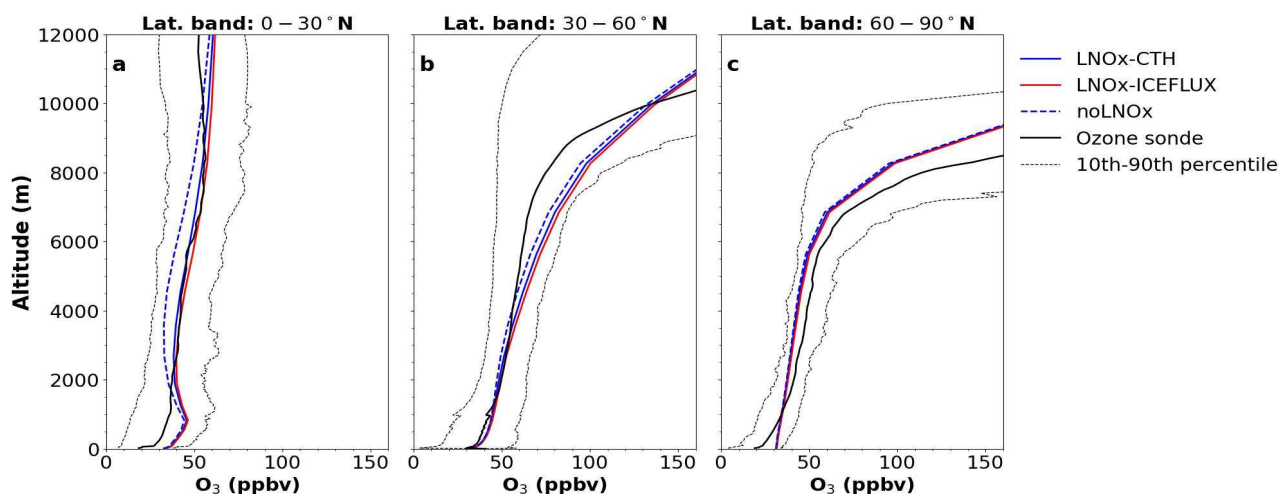
Figure 6. Vertical profile of annual mean of O_3 mixing ratio from noLNOx (blue dashed line), LNOx-CTH (blue solid line) and LNOx-ICEFLUX (red solid line) simulations and comparison with the WOUDC ozone-sonde measurements (black solid line), averaged for the stations over the latitude bands (a) 0°–30° N, (b) 30° N–60° N and (c) 60° N–90° N; the black dashed lines indicate the 10 and 90 percentiles of the WOUDC ozone-sonde measured values.

We also compare the vertical profiles of simulated O_3 with that from SHADOZ ozone-sonde measured data at stations of

440 Kuala Lampur, Hanoi, Costa Rica and Hilo, situated over the NH tropics. The plots are provided in supplementary material (Figure S1). Among the stations, at Kuala Lampur, the simulated O_3 profile from LNOx-ICEFLUX shows a good match with the observations at free troposphere, while the profile from LNOx-CTH aligns well with observations at Costa Rica. However the modelled O_3 profiles show under- and overestimation at most of the altitudes, respectively at Hanoi and Hilo, but overall

replicate the observed altitudinal distribution quite well. The comparisons once again represents the effect of LNOx on O$_3$, specifically at the free troposphere.
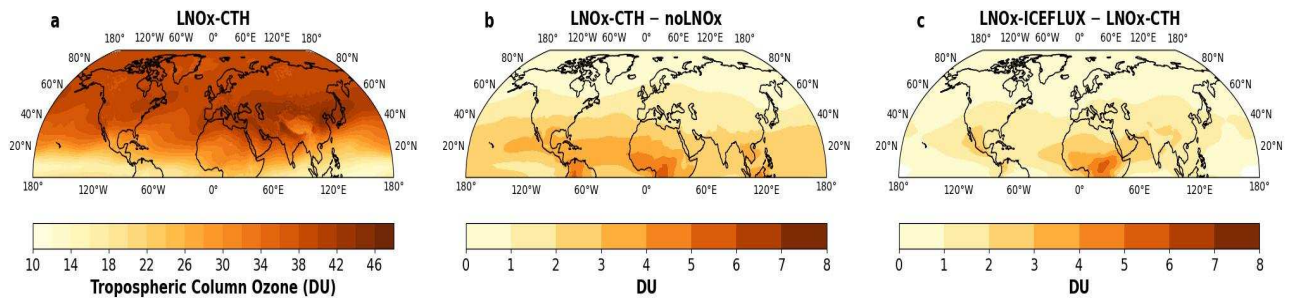
Figure 7. (a–c) Spatial distribution of (a) simulated tropospheric column of ozone (TCO) in DU, over the NH from experiment LNOx-CTH, (b) changes in simulated TCO from experiment LNOx-CTH w. r. t. noLNOx simulation, (c) differences in simulated TCO from experiment LNOx-ICEFLUX w. r. t. LNOx-CTH; positive and negative values represent the increase and decrease, respectively.
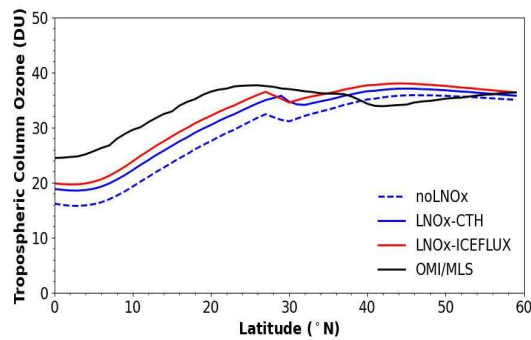
Figure 8. Zonal average of TCO from simulations over NH and their comparison with the same from OMI/MLS.

The monthly comparison of simulated O$_3$ from the LNOx-CTH and LNOx-ICEFLUX experiments with WOUDC ozone-sonde measurements, is presented in Figure S2 in the supplementary material, across two altitude (750–500 hPa and 500–200 hPa) and three latitude bands. The monthly variation reveals the highest peaks during March and October in the tropics, with the lowest levels observed during June–July for both altitude bands. A similar variation is noted at mid-latitudes and in the polar regions for the 750–500 hPa altitude band, aligning well with the observed monthly trends. The simulated O$_3$ from both experiments closely matches the observed values at the tropics and mid-latitudes for both altitude bands, exhibiting a low bias of ±3–10 ppbv. However, an overestimation of simulated O$_3$ is apparent during January–April, particularly over the tropics. While there is a good agreement between simulated and observed O$_3$ over the polar region for the 750–500 hPa altitude band, a significant underestimation of simulated O$_3$ is evident in the 500–200 hPa altitude band as discussed previously.

The spatial distribution of tropospheric column of ozone (TCO) from the LNOx-CTH simulation, along with the changes in TCO relative to the noLNOx and LNOx-ICEFLUX simulations, are shown in Figure 7. The TCO is observed to increase from the tropics toward higher latitudes, with the higher values occurring over the mid-latitudes (32–42 DU), particularly over Asian

countries (40–44 DU; Figure 7a). The lower TCO values in the tropics are attributed to the model's top height being lower than the tropopause height in this region (refer to the Table S1 in supplementary material presenting the tropopause height). The TCO from the LNOx-CTH simulation is higher by 2-4 DU at tropics, than that from the noLNOx simulation, while the LNOx-ICEFLUX simulation produces even higher TCO values compared to LNOx-CTH, especially over the tropics (Figures 7b–7c). The tropospheric O_3 burdens, estimated from the simulation LNOx-CTH and LNOx-ICEFLUX, are respectively 176 (150) Tg and 182 (155) Tg, over the NH and over the domain of 0°–60°N (presented inside parenthesis). These burdens represent a 7%–11% increase relative to the noLNOx simulation (Table 8). Notably, the estimated O_3 burden in this study aligns closely with observations from OMI/MLS (159 Tg) for the domain of 0°–60°N. The spatial distribution of TCO from OMI/MLS is shown in Figure S3 in supplementary material. A comparison of the zonal mean TCO over 0°–60°N reveals good agreement between the simulated TCO and OMI/MLS observations in the mid-latitudes (Figure 8). However, the simulations underestimate TCO in the tropics by 7%–26%, owing to the limited model top height, which excludes part of the troposphere above it. Despite this limitation, incorporating LNOx into the model leads to significant improvements in simulated TCO.

3.3.2 NO$_2$

Figure 9a represents the spatial distribution of NO$_2$ column density estimated from LNOx-CTH. 2–3 $\times$ 10^{15} molecules cm^{-2} NO$_2$ column densities are observed over the southern and eastern Asia (India and eastern China), north-west Europe and eastern part of USA. The spatial variation in NO$_2$ column matches well with that obtained from OMI observations (Figure S4 in supplementary material), highlighting elevated NO$_2$ column densities in countries with significant industrial activities (Cooper et al., 2022). However a decrease in NO$_2$ column density (0.2–0.6 $\times$ 10^{15} molecules cm^{-2}) is observed over the above mentioned continents due to inclusion of LNOx in model (Figure 9b). LNOx primarily produces NO, which rapidly oxidizes to form NO$_2$ in the presence of O$_3$, initially increasing the NO$_2$ level. However, rapid photolysis of NO$_2$ and its reaction with OH accelerate its conversion to HNO$_3$, leading to subsequent removal and a net decrease in NO$_2$ concentration (Labrador et al., 2005; Schumann and Huntrieser, 2007). Again, small increases of 0.1–0.2 $\times$ 10^{15} molecules cm^{-2} are observed over Africa, South America, and tropical oceans. Notably, NO$_2$ column densities from LNOx-ICEFLUX are higher by 1.0–1.2 $\times$ 10^{15} molecules cm^{-2} compared to LNOx-CTH over southern Asia, central Africa, and parts of the United States (Figure 9c).

The zonally averaged NO$_2$ column distribution (Figure 10) reveals elevated column densities over the tropics, especially between 20°–30°N, and the mid-latitudes, even in the absence of LNOx emissions. The zonal averages range from 0.35–1.75 $\times$ 10^{15} molecules cm^{-2} in these regions, which is nearly double the values observed at higher latitudes (60°–90°N). The peak at 20°–30°N is, however not observed in satellite observations. The higher uncertainty in tropospheric NO$_2$ columns retrieved from OMI observations is attributed to the complexity of tropospheric processes and the sensitivity of retrievals towards pollution levels (Bucsela et al., 2013). The simulations also identify a secondary maximum in NO$_2$ column density at 35°–45°N, which aligns with satellite observations over the mid-latitudes. At higher latitudes, where the magnitudes are comparatively lower, the simulated NO$_2$ column density matches well with satellite-based observations. Overall, the zonally averaged NO$_2$ column densities from the simulations closely replicate satellite observations, except for a pronounced peak at 20°–30°N from simulated NO$_2$. The tropospheric burden of NO$_2$ is 146 Gg from LNOx-CTH, being comparable to that from

noLNOx and 11% lower than that estimated from OMI (Table 8). The burden estimated from LNOx-ICEFLUX is 18% and 5% higher than the LNOx-CTH and OMI, respectively.
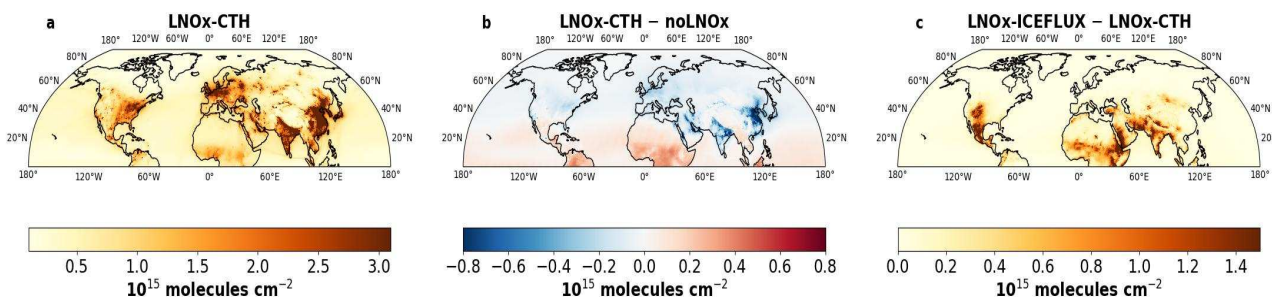
Figure 9. (a–c) Spatial distribution of (a) simulated NO_2 column density in $10^{15} \times$ molecules cm^{-2}, over the NH from experiment LNOx-CTH, (b) changes in simulated NO_2 column density from experiment LNOx-CTH w. r. t. noLNOx simulation, (c) differences in simulated NO_2 column density from experiment LNOx-ICEFLUX w. r. t. LNOx-CTH; positive and negative values represent the increase and decrease, respectively.
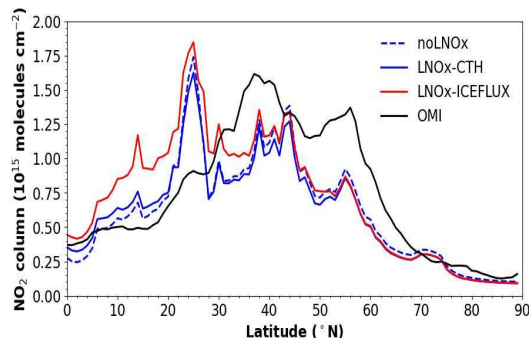
Figure 10. Zonal average of NO_2 column density from simulations over NH and their comparison with the same from OMI.

3.4 Impacts of LNOx on surface-level O_3 and NO_2

495 The effect of LNOx on surface level O_3 and NO_2 over NH is analysed in this section. The spatial distribution of the annual mean of O_3 mixing ratio and NO_2 at the surface from experiment LNOx-CTH and changes in the mixing ratio due to inclusion of LNOx (ΔO_3 and ΔNO_2), are presented in Figures 11a, 11d and 11b, 11e, respectively. Other than natural sources (e.g., lightning, soil-NOx emissions), emissions from fossil fuel combustion for transportation, industrial activities, energy generation and biomass burning also have a profound influence on tropospheric O_3 and NO_2 concentrations (Lelieveld and Dentener, 500 2000; van der A et al., 2008; Butler et al., 2020). In our study, the O_3 mixing ratio at the surface varies spatially with higher values ranging between 35–45 ppbv over the latitude band of $10°$–$50°$N, specifically over the lands, being almost 1.5–2 times of that observed over the rest of the NH. The NO_2 at the surface, is within a range of 0.5–2 ppbv over most parts of the NH showing higher magnitudes over USA, western Europe, India, eastern China and Japan (5–10 ppbv). To indicate the impact of

LNOx emissions on changes in surface-level O_3 and NO_2, annual mean of mixing ratio obtained from experiment LNOx–CTH is compared with respect to that from noLNOx. The positive and negative values of ΔO_3 and ΔNO_2 depict an increase and decrease, respectively, in surface mixing ratio (Figures 11b and 11e). The study shows an overall increase in surface O_3 by 1–3 ppbv over most parts of the tropical lands and mid-latitudes up to 50°N (Figure 11b), while the increase is almost negligible over 50°–90°N (<1 ppbv). A comparatively larger increase by 3–5 ppbv is observed over tropical parts of America and Africa and the Tibetan Plateau, but is particularly noteworthy (5–10 ppbv) over the central part of Africa, which is a hotspot location with high lightning flash rate (Section 3.1). Unlike O_3, NO_2 exhibits both increase and decrease in mixing ratio at the surface as an effect of lightning (Figure 11e), but by a lesser magnitude (0.01–0.1 ppbv). While the increase is observed over South America, Africa, the Maritime Continent and south-east Asia, a decrease in NO_2 mixing ratio is also there over India, southwest Asia and most of the continents north of 30°N. O_3 and NO_2, both exhibit a slight increase over the Atlantic and Pacific oceans in the tropics. The magnitudes and spatial patterns of ΔO_3 and ΔNO_2 from our study bear a resemblance to those from recent studies (Murray, 2016; Li et al., 2022; Cheng et al., 2024). The impact on surface O_3 and NO_2 concentrations is a localized effect of thunderstorms, crucially influenced by the specific photochemical conditions in the area (Murray, 2016). An increase in surface O_3 levels due to LNOx suggests the NOx concentration to be below the titration threshold (Pawar et al., 2012b).
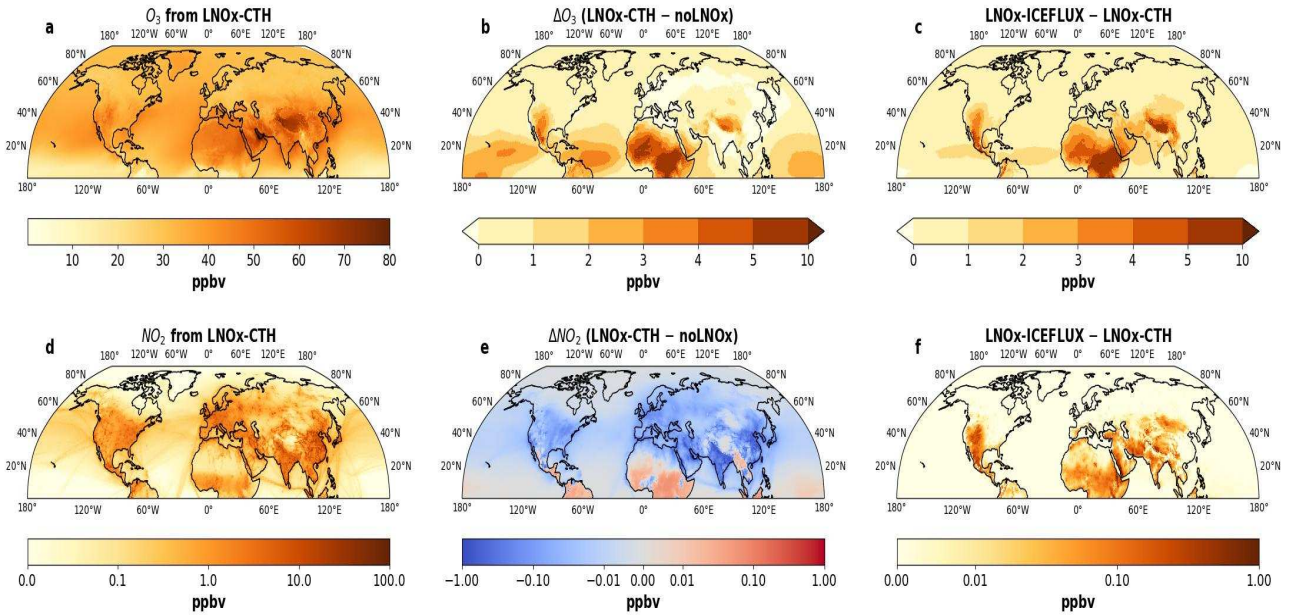
Figure 11. (a, d) Spatial distribution of annual mean mixing ratio in ppbv at the surface over NH from experiment LNOx-CTH for (a) O_3, (d) NO_2; (b, e) changes in mixing ratio at the surface due to inclusion of LNOx emissions for (b) O_3, (e) NO_2, positive and negative values show an increase and decrease, respectively; (c, f) differences in mixing ratio at the surface from experiment LNOx-ICEFLUX w. r. t. LNOx-CTH for (c) O_3, (f) NO_2.

The statistical analyses are also done comparing the simulated mixing ratios at surface to the observations and presented in Table 6. The agreement between simulated and observed O_3 is considered good, as indicated by lower values of RMSE (10.7–11 ppbv), MAB (6.5–7.1 ppbv), and NME (26.9%–27.8%). In contrast, the comparison for simulated NO_2 with observations shows higher NME (51.5%–52.7%). Figures S5(a–d) in supplementary material represent the absolute bias in the simulated annual mean of O_3 and NO_2 at the surface from experiment LNOx-CTH and LNOx-ICEFLUX, compared to the observations at available stations over the NH. The simulated O_3 and NO_2 mixing ratio is close enough to the observations at most of the stations over Europe and China, and also over the USA for O_3 and Canada and south America for NO_2. Higher bias for O_3 is, nonetheless, observed at stations over Canada, South America and few stations over eastern China. However, the inclusion of LNOx does not significantly impact the statistical scores. A detailed analysis of the altitude-wise changes in the mixing ratio of O_3, due to the impact of LNOx, is therefore necessary and has already been discussed in the Sections 3.3.1 and 3.3.2.

Table 6. Statistical analysis comparing simulated mixing ratio at surface to the ground-based observations for O_3 and NO_2

	Mean observed surface conc. over NH (ppbv)	Total number of stations	noLNOx			LNOx-CTH			LNOx-ICEFLUX		
			RMSE (ppbv)	MAB** (ppbv)	NME (%)	RMSE (ppbv)	MAB** (ppbv)	NME (%)	RMSE (ppbv)	MAB** (ppbv)	NME (%)
O_3	32.48	5185	10.9	6.5	27.3	10.7	6.5	26.9	11.0	7.1	27.8
NO_2	14.3	3857	9.2	6.4	51.5	9.3	6.6	52.7	9.3	6.6	52.7

**The positive and negative values of MAB represent respectively, modelled fields are higher and lower than the measurements.

3.5 Impacts on tropospheric OH burden and CH_4 lifetime

We also have evaluated the effects of LNOx on tropospheric chemistry in terms of changes in the burden of a major oxidant (OH) and the lifetime of trace gas CH_4. Table 7 illustrates the concentration of OH from experiment LNOx-CTH and the changes in concentration of OH with respect to that from noLNOx averaged over selected latitude and altitude bands. The OH concentration from the LNOx-ICEFLUX is also compared with that from LNOx-CTH in Table 7. The OH concentration in our study, over the tropics, is almost twice and 6–7 times higher than that over mid-latitudes and polar regions, respectively, which is consistent with the study by Mao et al. (2021). Again these concentrations are close enough to those values obtained in a multi-model study by Naik et al. (2013), but shows a higher OH concentration at tropical mid-troposphere (22–26×10^5 molecules cm^{-3}), unlike the studies by Naik et al. (2013); Luhar et al. (2021). Higher OH concentration in the upper troposphere is reported by Banerjee et al. (2014), due to transportation of water vapour through convection to the upper troposphere promoting the OH production due to reaction of exited state oxygen with water vapour. The annual mean OH concentration over NH, from our study, is 14.5×10^5 and 15.4×10^5 molecules cm^{-3} from LNOx-CTH and LNOx-ICEFLUX, respectively, being 6.6% and 13.2% higher than that obtained from noLNOx simulation (Table 8). The annual mean OH concentration is higher by 30%–38% in comparison to the multi-model mean obtained from ACCMIP simulations ($11.1\pm1.8 \times 10^5$ molecules cm^{-3}; Naik et al., 2013; Voulgarakis et al., 2013). We find an increase in OH concentration due to LNOx, which is again the largest over free troposphere at tropics (11%–28%), followed by mid-latitudes (Table 7). A 5%–7% higher OH concentration is also observed from LNOx-ICEFLUX in comparison to that from LNOx-CTH at the free troposphere. A warmer atmosphere at tropics and high humidity favour the increase in OH and a faster OH to CH_4 reaction, causing a shorter CH_4 lifetime at

these regions (Voulgarakis et al., 2013). The geographical distribution of changes in OH due to lightning is usually effected by the lightning parameterization used (Gordillo-Vázquez et al., 2019). The spatial distribution of changes in simulated OH concentration from LNOx-CTH w. r. t. noLNOx and from LNOx-ICEFLUX w. r. t. LNOx-CTH, at selected altitude bands, are also presented, respectively in Figures S6 and S7 in the supplementary material. The OH burden over NH is increased by 14% and 24% in LNOx-CTH and LNOx-ICEFLUX, respectively, from 0.082 Gg, estimated in simulation noLNOx (Table 8). In our study, we have estimated CH_4 lifetime (τ_{CH_4}) due to chemical loss, mainly due to reaction with OH. The average lifetime over NH are 4.84 and 4.5 years, as obtained respectively from experiments LNOx-CTH and LNOx-ICEFLUX, which are reduced respectively by 11% and 17% compared to the estimate from the noLNOx simulation (Table 8). The CH_4 lifetime as estimated from previous modelling studies, is within a range of 7–14 years (Naik et al., 2013; Lelieveld et al., 2016) and is visibly underestimated in our study. The underestimation in CH_4 lifetime in our study is due to the overestimation of OH concentrations, which promote the oxidation of CH_4, reducing the burden and increasing the chemical loss of CH_4, even in the absence of LNOx. Therefore, the underestimated CH_4 lifetime in the present study is not attributed to LNOx but likely stems from other factors including issues related to deficiencies in the chemistry or photolysis schemes. Addressing and resolving this issue will require further investigation in future studies. The CH_4 lifetime is underestimated especially over tropics showing values of 2–4 years (Figure S8 in supplementary material). The lifetime increases with higher latitudes and is maximum at polar region (40–60 years), which matches well with the estimated values from the study by Lelieveld et al. (2016), over higher latitudes (45°–90°N).

Table 7. Analysis of simulated OH concentration averaged over selected latitude and altitude bands. ΔOH represents changes in OH from experiment 'LNOx-CTH' w. r. t. that from experiment 'noLNOx'; positive and negative values represent the increase and decrease in OH concentration, respectively.

Latitude band	0°–30° N	30° N–60° N	60° N–90° N	0°–30° N	30° N–60° N	60° N–90° N	0°–30° N	30° N–60° N	60° N–90° N
Altitude band (hPa)	OH concentration (10^5 molecules cm^{-3}) from LNOx-CTH			ΔOH (%)			LNOx-ICEFLUX − LNOx-CTH (%)		
500–200	15.1	7.3	2.6	20.8	7.3	−3.7	5.2	2.6	1.5
750–500	26.0	11.3	3.1	28.7	8.6	−6.1	7.6	3.5	1.7
900–750	22.4	11.9	3.2	11.4	0	−3.0	5.8	2.6	1.1
998–900	19.5	13.4	2.8	2.1	−2.9	−3.7	4.2	1.9	0.8

Table 8. Tropospheric O_3, NO_2, OH burden and CH_4 lifetime from simulation experiments. The numbers within parenthesis represent the tropospheric O_3 burden over the domain from 0°–60°N.

	noLNOx	LNOx-CTH	LNOx-ICEFLUX
O_3 burden (Tg)[†]	164 (138)	176 (150)	182 (155)
NO_2 burden (Gg)[††]	146	146	172
OH concentration (molecules cm^{-3})	13.6×10^5	14.5×10^5	15.4×10^5
OH burden (Gg)	0.082	0.094	0.102
CH_4 lifetime due to chemical loss (yr)	5.45	4.84	4.5

[†]Tropospheric O_3 burden from OMI/MLS, estimated over the domain 0°–60°N, is 159 Tg.
[††]Tropospheric NO_2 burden over NH from OMI is 164 Gg.

Conclusion

565   This study evaluates the incorporation of lightning-produced NOx (LNOx) into the CHIMERE chemistry-transport model to assess its impact on tropospheric ozone (O_3) over the Northern Hemisphere (NH). A classical lightning parameterization based on cloud top height (CTH), developed by Price and Rind (1992), is applied (experiment: LNOx-CTH) with modifications to better align modelled flash rates over lands and oceans to satellite observations. Additionally, flash rates are computed using an updated ice flux based lightning scheme (experiment: LNOx-ICEFLUX; Finney et al., 2014). We perform a detailed evaluation

570   of model simulations, integrating in situ measurements and satellite observations to critically assess the reliability and applicability of these parameterizations. The annual flash frequencies over the NH are 20.7 and 21.6 flashes s^{-1} as estimated from the LNOx-CTH and LNOx-ICEFLUX experiments, respectively. For LNOx-ICEFLUX, a correction factor of 5 is applied to the simulated annual flash frequencies. The estimated LNOx emissions are 2.8 and 3.1 Tg N yr^{-1} from LNOx-CTH and LNOx-ICEFLUX experiments, respectively. Our study provides a comparative assessment of these two lightning parameterizations,

575   evaluating their influence on modelled lightning flashes, LNOx emissions and tropospheric distribution of O_3 and trace gases, with implications for improving both the parameterizations and the overall model.

     The major outcomes from our study are delineated here. Annual flash rates in tropical land and NH regions from both experiments, as well as in mid-latitudes from LNOx-ICEFLUX, show good agreement with satellite observations. Both the ICEFLUX and CTH schemes as implemented in CHIMERE, reproduce the seasonal cycle of lightning flash rates correctly

580   over the lands. LNOx emission peak during May–August, contributing 60%–70% of the total annual emissions, with most emissions concentrated in the tropics and mid-latitudes, and 60%–65% occurring in the mid-tropospheric region. The inclusion of LNOx emissions in CHIMERE significantly improves the simulated tropospheric O_3 distribution, particularly in the free troposphere over the tropics. A significant bias at the upper troposphere and lower stratosphere at higher latitudes, however highlights the necessity of improving the representation of stratosphere-troposphere exchange processes in the model. The

585   model adequately simulates the O_3 and NO_2 burden over the NH compared to satellite observations, showing a 7%–11% increase in O_3 burden from 164 Tg, due to the inclusion LNOx. Additionally, it leads to a 14%–24% increase in OH burden from 0.082 Gg and a 11%–17% reduction in CH_4 lifetime compared to the without LNOx scenario, though there remains scope for refining OH-related chemistry.

     Our study underscores that, despite its simple representation, the CTH scheme better captures the spatial variability of flashes

590   compared to satellite observations, outperforming the ICEFLUX scheme. However, the limitations of the CTH scheme in capturing mid-latitude flashes underscore the efficacy of the ICEFLUX scheme in these areas. Additionally, improving convective parameterization is crucial for better representation of oceanic flash rates. The ICEFLUX scheme also faces challenges in accurately simulating high-energy, less frequent flashes over oceans, emphasizing the need to incorporate additional factors alongside ice flux. The challenges to constrain parameters, such as cloud ice content and updraft mass flux, which are utilized in

595   flux-based lightning schemes, continue due to limited available observations. A recent study by Cummings et al. (2024), which have evaluated eighteen lightning parameterization schemes, demonstrates that those based on storm kinematics and structure performed better than the microphysical schemes, in their study. Developing integrated parameterizations that incorporate both

storm kinematics and microphysical processes, along with improved observational constraints, may provide a more robust and accurate representation of lightning flash rates, particularly in complex storm environments.

600 *Code and data availability.* The CHIMERE model (v2023r2) is available on the website at https://www.lmd.polytechnique.fr/chimere/. The in situ measurements and satellite data used in the study are all freely downloadable from cited URLs.

Author contributions. SG analysed the model output and data, downloaded satellite data, made plots, conceptualised and prepared a original version of the manuscript. AC performed the simulations and contributed to the measurement data collection. All co-authors have participated in conceptualisation of the study, the interpretation and discussion of the results, and the drafting of the final manuscript.

605 *Competing interests.* The authors declare that they have no conflict of interest.

Acknowledgements. This study was supported by the Agence de l'Environnement et de la Maîtrise de l'Energie (ADEME) within the framework of the ESCALAIR project (grant: 2162D0017). We also acknowledge the use of computational resources provided by the GENCI GEN10274 project.

References

Akimoto, H. and Tanimoto, H.: Rethinking of the adverse effects of NOx-control on the reduction of methane and tropospheric ozone–challenges toward a denitrified society, Atmospheric Environment, 277, 119 033, https://doi.org/10.1016/j.atmosenv.2022.119033, 2022.

Albrecht, R. I., Goodman, S. J., Buechler, D. E., Blakeslee, R. J., and Christian, H. J.: Where Are the Lightning Hotspots on Earth?, Bulletin of the American Meteorological Society, 97, 2051–2068, https://doi.org/10.1175/BAMS-D-14-00193.1, 2016.

Alfaro, S. C. and Gomes, L.: Modeling mineral aerosol production by wind erosion: Emission intensities and aerosol size distributions in source areas, Journal of Geophysical Research: Atmospheres, 106, 18 075–1808, https://doi.org/10.1029/2000JD900339, 2001.

Allen, D., Pickering, K., Stenchikov, G., Thompson, A., and Kondo, Y.: A three-dimensional total odd nitrogen (NOy) simulation during SONEX using a stretched-grid chemical transport model, Journal of Geophysical Research: Atmospheres, 105, 3851–3876, https://doi.org/10.1029/1999JD901029, 2000.

Allen, D., Pickering, K., Duncan, B., and Damon, M.: Impact of lightning NO emissions on North American photochemistry as determined using the Global Modeling Initiative (GMI) model, Journal of Geophysical Research: Atmospheres, 115, 2010.

Allen, D. J. and Pickering, K. E.: Evaluation of lightning flash rate parameterizations for use in a global chemical transport model, Journal of Geophysical Research: Atmospheres, 107, ACH–15, https://doi.org/10.1029/2002JD002066, 2002.

Banerjee, A., Archibald, A. T., Maycock, A. C., Telford, P., Abraham, N. L., Yang, X., Braesicke, P., and Pyle, J. A.: Lightning NOx, a key chemistry–climate interaction: impacts of future climate change and consequences for tropospheric oxidising capacity, Atmospheric Chemistry and Physics, 14, 9871–9881, 2014.

Bessagnet, B., Menut, L., Curci, G., Hodzic, A., Guillaume, B., Liousse, C., Moukhtar, S., Pun, B., Seigneur, C., and Schulz, M.: Regional modeling of carbonaceous aerosols over Europe–focus on secondary organic aerosols, Journal of Atmospheric Chemistry, 61, 175–202, https://doi.org/10.1007/s10874-009-9129-2, 2008.

Blakeslee, R. J., Lang, T. J., Koshak, W. J., Buechler, D., Gatlin, P., Mach, D. M., Stano, G. T., Virts, K. S., Walker, T. D., Cecil, D. J., Ellett, W., Goodman, S. J., Harrison, S., Hawkins, D. L., Heumesser, M., Lin, H., Maskey, M., Schultz, C. J., Stewart, M., Bateman, M., Chanrion, O., and Christian, H.: Three Years of the Lightning Imaging Sensor Onboard the International Space Station: Expanded Global Coverage and Enhanced Applications, Journal of Geophysical Research: Atmospheres, 125, e2020JD032 918, https://doi.org/10.1029/2020JD032918, 2020.

Boccippio, D. J.: Lightning Scaling Relations Revisited, Journal of the Atmospheric Sciences, 59, 1086–1104, https://doi.org/10.1175/1520-0469(2002)059<1086:LSRR>2.0.CO;2, 2002.

Boccippio, D. J., Cummins, K. L., Christian, H. J., and Goodman, S. J.: Combined satellite-and surface-based estimation of the intracloud–cloud-to-ground lightning ratio over the continental United States, Monthly Weather Review, 129, 108–122, https://doi.org/10.1175/1520-0493(2001)129<0108:CSASBE>2.0.CO;2, 2001.

Bucsela, E., Krotkov, N., Celarier, E., Lamsal, L., Swartz, W., Bhartia, P., Boersma, K., Veefkind, J., Gleason, J., and Pickering, K.: A new stratospheric and tropospheric NO 2 retrieval algorithm for nadir-viewing satellite instruments: applications to OMI, Atmospheric Measurement Techniques, 6, 2607–2626, https://doi.org/10.5194/amt-6-2607-2013, 2013.

Bucsela, E. J., Pickering, K. E., Allen, D. J., Holzworth, R. H., and Krotkov, N. A.: Midlatitude Lightning NOx Production Efficiency Inferred From OMI and WWLLN Data, Journal of Geophysical Research: Atmospheres, 124, 13 475–13 497, https://doi.org/10.1029/2019JD030561, 2019.

645   Burkholder, J. B., Sander, S. P., Abbatt, J., Barker, J. R., Cappa, C., Crounse, J. D., Dibble, T. S., Huie, R. E., Kolb, C. E., Kurylo, M. J., Orkin, V. L., Percival, C. J., Wilmouth, D. M., and Wine, P. H.: Chemical Kinetics and Photochemical Data for Use in Atmospheric Studies, Evaluation No. 19, Jet Propulsion Laboratory, Pasadena, http://jpldataeval.jpl.nasa.gov, 2019.

Butler, T., Lupascu, A., and Nalam, A.: Attribution of ground-level ozone to anthropogenic and natural sources of nitrogen oxides and reactive carbon in a global chemical transport model, Atmospheric Chemistry and Physics, 20, 10 707–10 731,
650   https://doi.org/10.5194/acp-20-10707-2020, 2020.

Carey, L. D., Koshak, W., Peterson, H., and Mecikalski, R. M.: The kinematic and microphysical control of lightning rate, extent, and NO production, Journal of Geophysical Research: Atmospheres, 121, 7975–7989, https://doi.org/10.1002/2015JD024703, 2016.

Cecil, D. J., Buechler, D. E., and Blakeslee, R. J.: Gridded lightning climatology from TRMM-LIS and OTD: Dataset description, Atmospheric Research, 135, 404–414, https://doi.org/10.1016/j.atmosres.2012.06.028, 2014.

655   Cheng, P., Pour-Biazar, A., Wu, Y., Kuang, S., McNider, R. T., and Koshak, W. J.: Utility of Geostationary Lightning Mapper-derived lightning NO emission estimates in air quality modeling studies, Atmospheric Chemistry and Physics, 24, 41–63, https://doi.org/10.5194/acp-24-41-2024, 2024.

Chin, M., Ginoux, P., Kinne, S., Torres, O., Holben, B. N., Duncan, B. N., Martin, R. V., Logan, J. A., Higurashi, A., and Nakajima, T.: Tropospheric Aerosol Optical Thickness from the GOCART Model and Comparisons with Satellite and Sun Photometer Measurements,
660   Journal of the Atmospheric Sciences, 59, 461–483, https://doi.org/10.1175/1520-0469(2002)059<0461:TAOTFT>2.0.CO;2, 2002.

Choi, Y., Wang, Y., Zeng, T., Martin, R. V., Kurosu, T. P., and Chance, K.: Evidence of lightning NOx and convective transport of pollutants in satellite observations over North America, Geophysical Research Letters, 32, https://doi.org/10.1029/2004GL021436, 2005.

Clark, S. K., Ward, D. S., and Mahowald, N. M.: Parameterization-based uncertainty in future lightning flash density, Geophysical Research Letters, 44, 2893–2901, https://doi.org/10.1002/2017GL073017, 2017.

665   Cooper, M. J., Martin, R. V., Hammer, M. S., Levelt, P. F., Veefkind, P., Lamsal, L. N., Krotkov, N. A., Brook, J. R., and McLinden, C. A.: Global fine-scale changes in ambient NO2 during COVID-19 lockdowns, Nature, 601, 380–387, https://doi.org/10.1038/s41586-021-04229-0, 2022.

Cummings, K., Pickering, K., Barth, M., Bela, M., Li, Y., Allen, D., Bruning, E., MacGorman, D., Ziegler, C., Biggerstaff, M., et al.: Evaluation of lightning flash rate parameterizations in a cloud-resolved WRF-Chem simulation of the 29–30 May 2012
670   Oklahoma severe supercell system observed during DC3, Journal of Geophysical Research: Atmospheres, 129, e2023JD039 492, https://doi.org/10.1029/2023JD039492, 2024.

Dahlmann, K., Grewe, V., Ponater, M., and Matthes, S.: Quantifying the contributions of individual NOx sources to the trend in ozone radiative forcing, Atmospheric Environment, 45, 2860–2868, https://doi.org/10.1016/j.atmosenv.2011.02.071, 2011.

Dufour, G., Hauglustaine, D., Zhang, Y., Eremenko, M., Cohen, Y., Gaudel, A., Siour, G., Lachatre, M., Bense, A., Bessagnet, B., et al.:
675   Recent ozone trends in the Chinese free troposphere: role of the local emission reductions and meteorology, Atmospheric Chemistry and Physics, 21, 16 001–16 025, https://doi.org/10.5194/acp-21-16001-2021, 2021.

Erdmann, F., Defer, E., Caumont, O., Blakeslee, R. J., Pédeboy, S., and Coquillat, S.: Concurrent satellite and ground-based lightning observations from the Optical Lightning Imaging Sensor (ISS-LIS), the low-frequency network Meteorage and the SAETTA Lightning Mapping Array (LMA) in the northwestern Mediterranean region, Atmospheric Measurement Techniques, 13, 853–875,
680   https://doi.org/10.5194/amt-13-853-2020, 2020.

Fehr, T., Höller, H., and Huntrieser, H.: Model study on production and transport of lightning-produced NOx in a EULINOX supercell storm, Journal of Geophysical Research: Atmospheres, 109, D09 102, https://doi.org/10.1029/2003JD003935, 2004.

Finney, D., Doherty, R., Wild, O., and Abraham, N. L.: The impact of lightning on tropospheric ozone chemistry using a new global lightning parametrisation, Atmospheric Chemistry and Physics, 16, 7507–7522, https://doi.org/10.5194/acp-16-7507-2016, 2016a.

685 Finney, D. L., Doherty, R. M., Wild, O., Huntrieser, H., Pumphrey, H. C., and Blyth, A. M.: Using cloud ice flux to parametrise large-scale lightning, Atmospheric Chemistry and Physics, 14, 12 665–12 682, https://doi.org/10.5194/acp-14-12665-2014, 2014.

Finney, D. L., Doherty, R. M., Wild, O., Young, P. J., and Butler, A.: Response of lightning NOx emissions and ozone production to climate change: Insights from the Atmospheric Chemistry and Climate Model Intercomparison Project, Geophysical Research Letters, 43, 5492–5500, https://doi.org/10.1002/2016GL068825, 2016b.

690 Ghosh, A., Patra, P. K., Ishijima, K., Umezawa, T., Ito, A., Etheridge, D. M., Sugawara, S., Kawamura, K., Miller, J. B., Dlugokencky, E. J., Krummel, P. B., Fraser, P. J., Steele, L. P., Langenfelds, R. L., Trudinger, C. M., White, J. W. C., Vaughn, B., Saeki, T., Aoki, S., and Nakazawa, T.: Variations in global methane sources and sinks during 1910–2010, Atmospheric Chemistry and Physics, 15, 2595–2612, https://doi.org/10.5194/acp-15-2595-2015, 2015.

Ghosh, R., Pawar, S. D., Hazra, A., Wilkinson, J., Mudiar, D., Domkawale, M. A., Vani, K. G., and Gopalakrishnan, V.: Sea-
695 sonal and Regional Distribution of Lightning Fraction Over Indian Subcontinent, Earth and Space Science, 10, e2022EA002 728, https://doi.org/10.1029/2022EA002728, 2023.

Goldenbaum, G. and Dickerson, R.: Nitric oxide production by lightning discharges, Journal of Geophysical Research: Atmospheres, 98, 18 333–18 338, https://doi.org/10.1029/93JD01018, 1993.

Gordillo-Vázquez, F. J., Pérez-Invernón, F. J., Huntrieser, H., and Smith, A. K.: Comparison of Six Lightning Parameterizations in CAM5
700 and the Impact on Global Atmospheric Chemistry, Earth and Space Science, 6, 2317–2346, https://doi.org/10.1029/2019EA000873, 2019.

Guenther, A. B., Jiang, X., Heald, C. L., Sakulyanontvittaya, T., Duhl, T., Emmons, L. K., and Wang, X.: The Model of Emissions of Gases and Aerosols from Nature version 2.1 (MEGAN2.1): an extended and updated framework for modeling biogenic emissions, Geoscientific Model Development, 5, 1471–1492, https://doi.org/10.5194/gmd-5-1471-2012, 2012.

Hasenkopf, C. A., Flasher, J. C., Veerman, O., and DeWitt, H. L.: OpenAQ: a platform to aggregate and freely share global air quality data,
705 in: AGU Fall Meeting Abstracts, vol. 2015, pp. A31D–0097, 2015.

Holle, R. L., Cummins, K. L., and Brooks, W. A.: Seasonal, Monthly, and Weekly Distributions of NLDN and GLD360 Cloud-to-Ground Lightning, Monthly Weather Review, 144, 2855–2870, https://doi.org/10.1175/MWR-D-16-0051.1, 2016.

Inness, A., Ades, M., Agustí-Panareda, A., Barré, J., Benedictow, A., Blechschmidt, A.-M., Dominguez, J. J., Engelen, R., Eskes, H., Flemming, J., Huijnen, V., Jones, L., Kipling, Z., Massart, S., Parrington, M., Peuch, V.-H., Razinger, M., Remy, S., Schulz,
710 M., and Suttie, M.: The CAMS reanalysis of atmospheric composition, Atmospheric Chemistry and Physics, 19, 3515–3556, https://doi.org/10.5194/acp-19-3515-2019, 2019.

Jourdain, L., Kulawik, S., Worden, H., Pickering, K., Worden, J., and Thompson, A.: Lightning NO x emissions over the USA constrained by TES ozone observations and the GEOS-Chem model, Atmospheric Chemistry and Physics, 10, 107–119, https://doi.org/10.5194/acp-10-107-2010, 2010.

715 Kang, D., Foley, K. M., Mathur, R., Roselle, S. J., Pickering, K. E., and Allen, D. J.: Simulating lightning NO production in CMAQv5. 2: performance evaluations, Geoscientific model development, 12, 4409–4424, https://doi.org/10.5194/gmd-12-4409-2019, 2019.

Kang, D., Mathur, R., Pouliot, G. A., Gilliam, R. C., and Wong, D. C.: Significant ground-level ozone attributed to lightning-induced nitrogen oxides during summertime over the Mountain West States, NPJ climate and atmospheric science, 3, 6, https://doi.org/10.1038/s41612-020-0108-2, 2020.

Koshak, W., Peterson, H., Biazar, A., Khan, M., and Wang, L.: The NASA Lightning Nitrogen Oxides Model (LNOM): Application to air quality modeling, Atmospheric Research, 135-136, 363–369, https://doi.org/10.1016/j.atmosres.2012.12.015, 2014.

Krider, E., Dawson, G., and Uman, M.: Peak power and energy dissipation in a single-stroke lightning flash, Journal of Geophysical Research, 73, 3335–3339, https://doi.org/10.1029/JB073i010p03335, 1968.

Labrador, L. J., von Kuhlmann, R., and Lawrence, M. G.: The effects of lightning-produced NOx and its vertical distribution on atmospheric chemistry: sensitivity simulations with MATCH-MPIC, Atmospheric Chemistry and Physics, 5, 1815–1834, https://doi.org/10.5194/acp-5-1815-2005, 2005.

Lamsal, L. N., Krotkov, N. A., Vasilkov, A., Marchenko, S., Qin, W., Yang, E.-S., Fasnacht, Z., Joiner, J., Choi, S., Haffner, D., et al.: Ozone Monitoring Instrument (OMI) Aura nitrogen dioxide standard product version 4.0 with improved surface and cloud treatments, Atmospheric Measurement Techniques, 14, 455–479, https://doi.org/10.5194/amt-14-455-2021, 2021.

Lelieveld, J. and Dentener, F. J.: What controls tropospheric ozone?, Journal of Geophysical Research: Atmospheres, 105, 3531–3551, https://doi.org/10.1029/1999JD901011, 2000.

Lelieveld, J., Gromov, S., Pozzer, A., and Taraborrelli, D.: Global tropospheric hydroxyl distribution, budget and reactivity, Atmospheric Chemistry and Physics, 16, 12 477–12 493, https://doi.org/10.5194/acp-16-12477-2016, 2016.

Levelt, P. F., Joiner, J., Tamminen, J., Veefkind, J. P., Bhartia, P. K., Stein Zweers, D. C., Duncan, B. N., Streets, D. G., Eskes, H., van der A, R., et al.: The Ozone Monitoring Instrument: overview of 14 years in space, Atmospheric Chemistry and Physics, 18, 5699–5745, https://doi.org/10.5194/acp-18-5699-2018, 2018.

Li, M., Mao, J., Chen, S., Bian, J., Bai, Z., Wang, X., Chen, W., and Yu, P.: Significant contribution of lightning NOx to summertime surface O3 on the Tibetan Plateau, Science of The Total Environment, 829, 154 639, https://doi.org/10.1016/j.scitotenv.2022.154639, 2022.

Liaskos, C. E., Allen, D. J., and Pickering, K. E.: Sensitivity of tropical tropospheric composition to lightning NOx production as determined by replay simulations with GEOS-5, Journal of Geophysical Research: Atmospheres, 120, 8512–8534, https://doi.org/10.1002/2014JD022987, 2015.

Luhar, A. K., Galbally, I. E., Woodhouse, M. T., and Abraham, N. L.: Assessing and improving cloud-height-based parameterisations of global lightning flash rate, and their impact on lightning-produced NO x and tropospheric composition in a chemistry–climate model, Atmospheric Chemistry and Physics, 21, 7053–7082, https://doi.org/10.5194/acp-21-7053-2021, 2021.

Luhar, A. K., Jones, A. C., and Wilkinson, J. M.: Quantifying the impact of global nitrate aerosol on tropospheric composition fields and its production from lightning NOx, Atmospheric Chemistry and Physics, 24, 14 005–14 028, https://doi.org/10.5194/acp-24-14005-2024, 2024.

Luo, C., Wang, Y., and Koshak, W. J.: Development of a self-consistent lightning NOx simulation in large-scale 3-D models, Journal of Geophysical Research: Atmospheres, 122, 3141–3154, https://doi.org/10.1002/2016JD026225, 2017.

Mailler, S., Menut, L., di Sarra, A. G., Becagli, S., Di Iorio, T., Bessagnet, B., Briant, R., Formenti, P., Doussin, J.-F., Gómez-Amo, J. L., Mallet, M., Rea, G., Siour, G., Sferlazzo, D. M., Traversi, R., Udisti, R., and Turquety, S.: On the radiative impact of aerosols on photolysis rates: comparison of simulations and observations in the Lampedusa island during the ChArMEx/ADRIMED campaign, Atmospheric Chemistry and Physics, 16, 1219–1244, https://doi.org/10.5194/acp-16-1219-2016, 2016.

Mao, J., Zhao, T., Keller, C. A., Wang, X., McFarland, P. J., Jenkins, J. M., and Brune, W. H.: Global Impact of Lightning-Produced Oxidants, Geophysical Research Letters, 48, e2021GL095 740, https://doi.org/10.1029/2021GL095740, 2021.

Maseko, B., Feig, G., and Burger, R.: Estimating lightning NOx production over South Africa, South African Journal of Science, 117, 1–11, https://doi.org/10.17159/sajs.2021/8035, 2021.

Menut, L., Bessagnet, B., Khvorostyanov, D., Beekmann, M., Blond, N., Colette, A., Coll, I., Curci, G., Foret, G., Hodzic, A., Mailler, S., Meleux, F., Monge, J. L., Pison, I., Siour, G., Turquety, S., Valari, M., Vautard, R., and Vivanco, M. G.: CHIMERE 2013: a model for regional atmospheric composition modelling, Geoscientific Model Development, 6, 981–1028, https://doi.org/10.5194/gmd-6-981-2013, 2013.

Menut, L., Bessagnet, B., Mailler, S., Pennel, R., and Siour, G.: Impact of lightning NOx emissions on atmospheric composition and meteorology in Africa and Europe, Atmosphere, 11, 1128, https://doi.org/10.3390/atmos11101128, 2020a.

Menut, L., Bessagnet, B., Siour, G., Mailler, S., Pennel, R., and Cholakian, A.: Impact of lockdown measures to combat Covid-19 on air quality over western Europe, Science of The Total Environment, 741, 140 426, https://doi.org/10.1016/j.scitotenv.2020.140426, 2020b.

Menut, L., Bessagnet, B., Briant, R., Cholakian, A., Couvidat, F., Mailler, S., Pennel, R., Siour, G., Tuccella, P., Turquety, S., and Valari, M.: The CHIMERE v2020r1 online chemistry-transport model, Geoscientific Model Development, 14, 6781–6811, https://doi.org/10.5194/gmd-14-6781-2021, 2021.

Menut, L., Cholakian, A., Pennel, R., Siour, G., Mailler, S., Valari, M., Lugon, L., and Meurdesoif, Y.: The CHIMERE chemistry-transport model v2023r1, Geoscientific Model Development Discussions, 2024, 1–44, https://doi.org/10.5194/gmd-17-5431-2024, 2024.

Michalon, N., Nassif, A., Saouri, T., Royer, J. F., and Pontikis, C. A.: Contribution to the climatological study of lightning, Geophysical Research Letters, 26, 3097–3100, https://doi.org/10.1029/1999GL010837, 1999.

Miyazaki, K., Eskes, H. J., Sudo, K., and Zhang, C.: Global lightning NOx production estimated by an assimilation of multiple satellite data sets, Atmospheric Chemistry and Physics, 14, 3277–3305, https://doi.org/10.5194/acp-14-3277-2014, 2014.

Monahan, E. C.: The Ocean as a Source for Atmospheric Particles, pp. 129–163, Springer Netherlands, https://doi.org/10.1007/978-94-009-4738-2_6, 1986.

Murray, L. T.: Lightning NOx and impacts on air quality, Current Pollution Reports, 2, 115–133, 2016.

Murray, L. T., Logan, J. A., and Jacob, D. J.: Interannual variability in tropical tropospheric ozone and OH: The role of lightning, Journal of Geophysical Research: Atmospheres, 118, 11–468, 2013.

Murray, L. T., Fiore, A. M., Shindell, D. T., Naik, V., and Horowitz, L. W.: Large uncertainties in global hydroxyl projections tied to fate of reactive nitrogen and carbon, Proceedings of the National Academy of Sciences, 118, e2115204 118, https://doi.org/10.1073/pnas.2115204118, 2021.

Naik, V., Voulgarakis, A., Fiore, A. M., Horowitz, L. W., Lamarque, J.-F., Lin, M., Prather, M. J., Young, P. J., Bergmann, D., Cameron-Smith, P. J., Cionni, I., Collins, W. J., Dalsøren, S. B., Doherty, R., Eyring, V., Faluvegi, G., Folberth, G. A., Josse, B., Lee, Y. H., MacKenzie, I. A., Nagashima, T., van Noije, T. P. C., Plummer, D. A., Righi, M., Rumbold, S. T., Skeie, R., Shindell, D. T., Stevenson, D. S., Strode, S., Sudo, K., Szopa, S., and Zeng, G.: Preindustrial to present-day changes in tropospheric hydroxyl radical and methane lifetime from the Atmospheric Chemistry and Climate Model Intercomparison Project (ACCMIP), Atmospheric Chemistry and Physics, 13, 5277–5298, https://doi.org/10.5194/acp-13-5277-2013, 2013.

Nault, B. A., Laughner, J. L., Wooldridge, P. J., Crounse, J. D., Dibb, J., Diskin, G., Peischl, J., Podolske, J. R., Pollack, I. B., Ryerson, T. B., Scheuer, E., Wennberg, P. O., and Cohen, R. C.: Lightning NOx Emissions: Reconciling Measured and Modeled Estimates With Updated NO Chemistry, Geophysical Research Letters, 44, 9479–9488, https://doi.org/10.1002/2017GL074436, 2017.

Ott, L. E., Pickering, K. E., Stenchikov, G. L., Allen, D. J., DeCaria, A. J., Ridley, B., Lin, R.-F., Lang, S., and Tao, W.-K.: Production of lightning NO and its vertical distribution calculated from three-dimensional cloud-scale chemical transport model simulations, Journal of Geophysical Research: Atmospheres, 115, D04 301, https://doi.org/https://doi.org/10.1029/2009JD011880, 2010.

795 Pawar, S. D., Lal, D. M., and Murugavel, P.: Lightning characteristics over central India during Indian summer monsoon, Atmospheric Research, 106, 44–49, https://doi.org/10.1016/j.atmosres.2011.11.007, 2012a.

Pawar, V., Pawar, S. D., Beig, G., and Sahu, S. K.: Effect of lightning activity on surface NOx and O_3 over a tropical station during pre-monsoon and monsoon seasons, Journal of Geophysical Research: Atmospheres, 117, D05 310, https://doi.org/10.1029/2011JD016930, 2012b.

800 Pérez-Invernón, F. J., Gordillo-Vázquez, F. J., Huntrieser, H., Jöckel, P., and Bucsela, E. J.: Sensitivity of climate-chemistry model simulated atmospheric composition to lightning-produced NOx parameterizations based on lightning frequency, EGUsphere, 2024, 1–26, https://doi.org/10.5194/egusphere-2024-3348, 2024.

Pickering, K. E., Wang, Y., Tao, W.-K., Price, C., and Müller, J.-F.: Vertical distributions of lightning NOx for use in regional and global chemical transport models, Journal of Geophysical Research: Atmospheres, 103, 31 203–31 216, https://doi.org/10.1029/98JD02651, 1998.

805 Price, C. and Rind, D.: A simple lightning parameterization for calculating global lightning distributions, Journal of Geophysical Research: Atmospheres, 97, 9919–9933, https://doi.org/10.1029/92JD00719, 1992.

Price, C. and Rind, D.: What determines the cloud-to-ground lightning fraction in thunderstorms?, Geophysical Research Letters, 20, 463–466, https://doi.org/10.1029/93GL00226, 1993.

Price, C. and Rind, D.: Modeling global lightning distributions in a general circulation model, Monthly Weather Review, 122, 1930–1939, 810 https://doi.org/10.1175/1520-0493(1994)122<1930:MGLDIA>2.0.CO;2, 1994.

Price, C., Penner, J., and Prather, M.: NOx from lightning: 1. Global distribution based on lightning physics, Journal of Geophysical Research: Atmospheres, 102, 5929–5941, https://doi.org/10.1029/96JD03504., 1997a.

Price, C., Penner, J., and Prather, M.: NOx from lightning: 2. Constraints from the global atmospheric electric circuit, Journal of Geophysical Research: Atmospheres, 102, 5943–5951, https://doi.org/10.1029/96JD02551, 1997b.

815 Pun, B. K. and Seigneur, C.: Investigative modeling of new pathways for secondary organic aerosol formation, Atmospheric Chemistry and Physics, 7, 2199–2216, https://doi.org/10.5194/acp-7-2199-2007, 2007.

Ren, Y., Xu, W., and Fu, J.: Characteristics of intracloud lightning to cloud-to-ground lightning ratio in thunderstorms over Eastern and Southern China, Atmospheric Research, 300, 107 231, https://doi.org/10.1016/j.atmosres.2024.107231, 2024.

Schumann, U. and Huntrieser, H.: The global lightning-induced nitrogen oxides source, Atmospheric Chemistry and Physics, 7, 3823–3907, 820 https://doi.org/10.5194/acp-7-3823-2007, 2007.

Tiedtke, M.: A comprehensive mass flux scheme for cumulus parameterization in large-scale models, Monthly Weather Reviews, 117, 1779–1800, https://doi.org/10.1175/1520-0493(1989)117<1779:ACMFSF>2.0.CO;2, 1989.

Tost, H., Jöckel, P., and Lelieveld, J.: Lightning and convection parameterisations ndash; uncertainties in global modelling, Atmospheric Chemistry and Physics, 7, 4553–4568, https://doi.org/10.5194/acp-7-4553-2007, 2007.

825 Troen, I. and Mahrt, L.: A simple model of the atmospheric boundary layer: Sensitivity to surface evaporation, Boundary-Layer Meteorology, 37, 129–148, https://doi.org/10.1007/BF00122760, 1986.

Uman, M. A.: The lightning discharge, Courier Corporation, 2001.

van der A, R. J., Eskes, H. J., Boersma, K. F., van Noije, T. P. C., Van Roozendael, M., De Smedt, I., Peters, D. H. M. U., and Meijer, E. W.: Trends, seasonal variability and dominant NOx source derived from a ten year record of NO2 measured from space, Journal of 830 Geophysical Research: Atmospheres, 113, D04 302, https://doi.org/10.1029/2007JD009021, 2008.

van Leer, B.: Towards the ultimate conservative difference scheme: IV. A new approach to numerical convection, Journal of Computational Physics, 23, 276–299, https://doi.org/10.1016/0021-9991(77)90095-X, 1977.

Verma, S., Yadava, P. K., Lal, D. M., Mall, R. K., Kumar, H., and Payra, S.: Role of Lightning NOx in Ozone Formation: A Review, Pure and Applied Geophysics, 178, 1425–1443, https://doi.org/10.1007/s00024-021-02710-5, 2021.

835 Vonnegut, B.: Some facts and speculations concerning the origin and role of thunderstorm electricity, pp. 224–241, American Meteorological Society, https://doi.org/10.1007/978-1-940033-56-3_11, 1963.

Voulgarakis, A., Naik, V., Lamarque, J.-F., Shindell, D. T., Young, P. J., Prather, M. J., Wild, O., Field, R. D., Bergmann, D., Cameron-Smith, P., Cionni, I., Collins, W. J., Dalsøren, S. B., Doherty, R. M., Eyring, V., Faluvegi, G., Folberth, G. A., Horowitz, L. W., Josse, B., MacKenzie, I. A., Nagashima, T., Plummer, D. A., Righi, M., Rumbold, S. T., Stevenson, D. S., Strode, S. A., Sudo, K., Szopa, S., and

840 Zeng, G.: Analysis of present day and future OH and methane lifetime in the ACCMIP simulations, Atmospheric Chemistry and Physics, 13, 2563–2587, https://doi.org/10.5194/acp-13-2563-2013, 2013.

Wesely, M.: Parameterization of Surface Resistances to Gaseous Dry Deposition in Regional-Scale Numerical Models, Atmospheric Environment, 23, 1293–1304, https://doi.org/10.1016/0004-6981(89)90153-4, 1989.

Wild, O., Zhu, X., and Prather, M. J.: Fast-J: Accurate Simulation of In- and Below-Cloud Photolysis in Tropospheric Chemical Models,

845 Journal of Atmospheric Chemistry, 37, 245–282, https://doi.org/10.1023/A:1006415919030, 2000.

Williams, E. R.: Large-scale charge separation in thunderclouds, Journal of Geophysical Research: Atmospheres, 90, 6013–6025, https://doi.org/10.1029/JD090iD04p06013, 1985.

Wu, Y., Pour-Biazar, A., Koshak, W., and Cheng, P.: LNOx emission model for air quality and climate studies using satellite lightning mapper observations, Journal of Geophysical Research: Atmospheres, 128, e2022JD037 406, https://doi.org/10.1029/2022JD037406, 2023.

850 Xu, M., Qie, X., Zhao, C., Yuan, S., Li, J., Tao, Y., Shi, G., Pang, W., and Shi, L.: Distribution of lightning spatial modes and climatic causes in China, Atmospheric and Oceanic Science Letters, 16, 100 338, https://doi.org/10.1016/j.aosl.2023.100338, 2023.

Zhang, D., Cummins, K. L., Lang, T. J., Buechler, D., and Rudlosky, S.: Performance Evaluation of the Lightning Imaging Sensor on the International Space Station, Journal of Atmospheric and Oceanic Technology, 40, 1063–1082, https://doi.org/10.1175/JTECH-D-22-0120.1, 2023.

855 Zhang, L., Gong, S., Padro, J., and Barrie, L.: A size-segregated particle dry deposition scheme for an atmospheric aerosol module, Atmospheric Environment, 35(3), 549–560, https://doi.org/10.1016/S1352-2310(00)00326-5, 2001.

Zhao, C., Wang, Y., Choi, Y., and Zeng, T.: Summertime impact of convective transport and lightning NOx production over North America: modeling dependence on meteorological simulations, Atmospheric Chemistry and Physics, 9, 4315–4327, https://doi.org/www.atmos-chem-phys.net/9/4315/2009/, 2009.

860 Zhao, Y., Saunois, M., Bousquet, P., Lin, X., Hegglin, M. I., Canadell, J. G., Jackson, R. B., and Zheng, B.: Reconciling the bottom-up and top-down estimates of the methane chemical sink using multiple observations, Atmospheric Chemistry and Physics, 23, 789–807, https://doi.org/10.5194/acp-23-789-2023, 2023.

Ziemke, J., Chandra, S., Duncan, B., Froidevaux, L., Bhartia, P., Levelt, P., and Waters, J.: Tropospheric ozone determined from Aura OMI and MLS: Evaluation of measurements and comparison with the Global Modeling Initiative's Chemical Transport Model, Journal of

865 Geophysical Research: Atmospheres, 111, https://doi.org/10.1029/2006JD007089, 2006.